Pre-explosive conduit conditions of the 1997 Vulcanian explosions at Soufrière Hills Volcano, Montserrat: I. Pressure and vesicularity distributions

Alain Burgisser, Stéphane Poussineau, Laurent Arbaret, Thomas Giachetti, Jean-Louis Bourdier

Pre-explosive conduit conditions of the 1997 Vulcanian explosions at Soufrière Hills

Volcano, Montserrat: I. Pressure and vesicularity distributions.

Alain BURGISSER[a*], Stéphane POUSSINEAU[a], Laurent ARBARET[a], Timothy H.

DRUITT[b], Thomas GIACHETTI[b], Jean-Louis BOURDIER[a]

[a] Institut des Sciences de la Terre d'Orléans,

CNRS, Université d'Orléans

1A rue de la Férollerie

45071 Orléans cedex 2 (France)

[b] Laboratoire Magmas et Volcans

Université Blaise Pascal, CNRS, and IRD

5, rue Kessler

63038 Clermont-Ferrand (France)

* Corresponding author: Tel: +33 238 25 53 89, Fax: +33 238 63 64 88. Email:
burgisse@cnrs-orleans.fr

Abstract

An authoritative case of Vulcanian eruptive dynamics is the series of 88 explosions that occurred between August and October 1997 at Soufrière Hills volcano on Montserrat Island. The state of the magmatic column just before a Vulcanian explosion is still poorly understood, but conditions the eruptive style. This study establishes such a pre-explosive stratigraphy by *1)* documenting the textures covering the range of the 1997 products, *2)* quantitative analysis of H_2O content in interstitial glass measured by Karl-Fischer Titration, and *3)* combining these data with a simple model linking pre- and post-explosive vesicularities. The model shows that syn-explosive degassing affects greatly the way porosity evolves by decompression during an explosion. The stratigraphy reconstruction shows a three-part vertical layering of the conduit prior to explosion with overall denser values than those previously suggested. A dense and strongly degassed plug caps the column. It is underlain by a shallow transition zone featuring complex mingling between vesicular and dense magma up to 10 MPa. At higher pressure, up to 80 MPa, lies a more homogeneous zone of relatively dense (10-20 vol%) magma, which was emplaced under partly open-system degassing. This conduit stratigraphy gives the vision of a strongly heterogeneous magma column immediately prior to its disruption. Our analysis suggests that fragmenting such a composite magma cannot happen in a single coherent pulse, but rather as stages. The transition zone contains heterogeneous amounts of exsolved gas that could explain the pulsatory nature of the Vulcanian jets at the beginning of the explosions. This contrasts with the nearly constant vesicularities of the deeper part of the pre-explosive magma column, which are propitious to a general, short-lived disruption.

Keywords: Soufrière Hills Volcano; Vulcanian explosions; water content; decompression; conduit modeling

1. Introduction

Vulcanian eruptions are generally short-lived (seconds to minutes) explosions that result from brutal decompression of a conduit containing pressurized magma and that eject relatively small volumes of material (Self et al., 1979; Woods, 1995; Stix et al., 1997; Morrissey and Mastin, 2000). An authoritative case of such eruptive dynamics is the series of 88 Vulcanian explosions that occurred with recurrence intervals of ~10 hours between August and October 1997 at Soufrière Hills Volcano on Montserrat Island (Young et al., 1998; Druitt et al., 2002). Each explosion started with a high-flux phase that lasted several tens of seconds, involving the discharge of on average $3x10^5$ m^3 of magma, about one-third forming fallout and two-third forming pyroclastic flows and surges (Druitt et al., 2002; Formenti et al., 2003; Formenti and Druitt, 2003; Clarke et al., 2002, 2007; Kennedy et al., 2005; Giachetti et al., accepted). A well-documented eruptive sequence, and a wealth of information on the dynamics of these explosions, contributed to establishing this Vulcanian episode as a reference, and the reader is referred to these papers for full details.

The state of the magmatic column just before a Vulcanian explosion holds key information for understanding why the eruption suddenly unfolds in an explosive fashion rather than by gently rebuilding a lava dome. Reconstructing this pre-explosive state requires linking melt volatile content, porosity, vesicle size distribution, and crystal textures preserved in the ejecta to those in the pre-explosive magma column. Only with this link can conduit stratigraphy be deduced from erupted products and used to approach the inner workings of Vulcanian explosion. Triggering is conditioned by pressurization mechanisms and plug formation, and in a companion paper we use the conduit stratigraphy established herein to assess both phenomena (Burgisser et al., submitted). Determining magma column stratigraphy immediately prior to its disruption fills a gap of knowledge, as previous studies have focused

on fossil conduits that preserve the unerupted magma column after eruption cessation (Eichelberger et al., 1986; Stasiuk et al., 1996; Keating et al., 2007).

The present study establishes such a pre-explosive stratigraphy by *1)* documenting interstitial glass H_2O contents and textures covering the range of the 1997 Vulcanian lithologies, *2)* using these water contents and results from a detailed work on vesicle textures and size distributions of the same sample suite (Giachetti et al., accepted) to deduce pre-explosive pressures, and *3)* combining these data with a simple physical model linking pre- and post-explosive clast porosity.

2. Materials and methods

2.1. Sampling and studied material

Representative ejecta from fountain-collapse pyroclastic flows and fallout deposits formed during the 1997 Vulcanian explosions of Soufrière Hills were collected in the summer of 2006. Sampling locations can be divided in three main sites (Fig. 1). All fallout pumices are from site 1, located at the top of St. Georges Hill (lat. 16.72205; long. 62.20759), and were collected in ash deposits. We analyzed only well preserved grey pumices from 1 to 3 cm in diameter to avoid secondary meteoric alteration effects such as acid rain. Pumices from pyroclastic flows were collected at two sites. One (site 2) is located in the north-eastern part of Plymouth (lat. 16.71338; long. 62.21340) and the other (site 3) between Bramble airport and Trant's village (lat. 16.75276; long. 62.16243). At each site, pumices were collected both on the ground surface and in pumice-flow deposits so as to gather the broadest range of macroscopic features. About 30 pumices >10 cm in size, and about 150 pumices between 16 and 32 mm, were selected for textural observation. We distinguished five main lithologies based on macroscopic features and depositional origin (Fig. 2). Four categories were collected

from pyroclastic flow deposits: 1) dark and glassy dense clasts, 2) texturally homogeneous pumices, 3) texturally heterogeneous pumices, and 4) breadcrusted bombs. The fifth category is composed of homogeneous pumices sampled in fallout deposits. Thirty-eight representative samples sorted according to these lithologies underwent further analysis. Clasts with heterogeneities caused by chemical composition, such as inclusions, were not considered.

2.2. Textural observations and analysis

Thin sections were imaged by classical optical microscopy for preliminary observations and sample selection, and by scanning electron microscopy (SEM) with a JEOL JSM-6400 microscope operating at 15 to 20 kV acceleration voltages (Polytech, Orléans University) for detailed microtextural observations. BackScattered Electrons (BSE) images were analyzed with the ImageJ software in order to measure the 2D modal proportion of bubbles, phenocrysts, microlites, and glass. Following Clarke et al. (2007), we defined crystals having a cross-section area $<\sim$500 μm^2 as microlites, larger crystals being phenocrysts. This choice is supported by the detailed crystal size distributions of some samples of the same suite (Giachetti et al., accepted). Bulk microlite contents were measured irrespective of mineralogy whereas plagioclase microlite contents consist of plagioclase crystals $<$500 μm^2. Manual segmentation was preferred to automatic segmentation because of the small electronic contrast in grey levels between interstitial glass and plagioclase. At least 3 SEM images per sample were used in order to minimize errors. Uncertainties on vesicularity and microlite contents were estimated to $\pm$10% and $\pm$5%, respectively. Glass proportions are given on a bubble-free basis, and microlite contents (bulk and plagioclase) are given with respect to the groundmass (bulk minus vesicles and phenocrysts). Bulk microlites were used to correct the bulk water contents and plagioclase microlite were used to calculate

pre-explosive pressures using the procedure of Clarke et al. (2007). We noted the presence of

silica precipitate in most samples (Fig. 3F), which we mostly avoided in our measurements as

it could hardly be segmented from the glass. When the precipitate was pervasive, we

considered it as glass, while noting that its proportion was always subordinate to that of the

glass. We measured the relative proportion of plagioclase phenocrysts (85 vol%, 2570 kg/m^3)

and pyroxene phenocrysts (15 vol%, 3300 kg/m^3) on a few representative samples, so as to

calculate an average crystal density of 2700 kg/m^3. The glass density, 2380±10 kg/m^3, was

measured by double weighing in water and ethanol of 10 chips of bubble-free and crystal-free

rhyolitic glass of a composition similar to that of the natural interstitial glass (VH, Table A1).

2.3. Glass H_2O contents by Karl-Fischer Titration

Measurement of water in interstitial volcanic glasses is an analytical challenge that

requires a complex technical procedure because of generally low H_2O contents and high

crystalline groundmasses. In the 1997 ejecta, interstitial glass areas are too small for FTIR

analysis (<5x4 µm) or ion probe analysis (<15x15 µm), and have low water contents (Harford

et al., 2003). Punctual micro-Raman analyses are hindered by the presence of numerous,

small Fe-Ti oxides that interfere spectrally with H_2O. Considering pumice characteristics and

laboratory facilities, we choose Karl Fischer Titration, which is a conventional bulk-

extraction method well adapted for the determination of very small amount of water in

volcanic rocks (Turek et al., 1976; Westrich, 1987).

During a Karl-Fischer Titration, H_2O reacts quantitatively, in presence of specific

reagents, with coulometrically generated iodine (Westrich, 1987; Holtz et al., 1992, 1995;

Behrens et al., 1996). The coulometer used for this study was a Mettler Toledo DL32.

Optimum conditions were reached when up to 100 µg of water were extracted from the rock

chip, which usually translated in melting chips of up to 50 mg. It was necessary to avoid water adsorption on our pumices because of their low water content, so samples were stored in a drying oven at 120°C for several days before titration. Titration using a single piece of rock and a crushed powder yielded nearly identical H_2O contents, which shows that crushing had no significant influence on measurements.

Samples were heated progressively from 20°C to 1300°C at ~150 °/min with an induction furnace. The extracted water was transported by a dry argon flux to the titration cell through a CuO oxidation furnace (oxidation of hydroxyl groups). The precision for H_2O bulk measurement, on the order of ±0.05 wt%, mainly depends on the amount of sample and the duration of the titration (10 min for this study, Table 1). Three titrations were performed on most samples to check reproducibility and sample homogeneity. Interstitial glass water contents were calculated for each titration by correcting bulk water contents for the presence of phenocrysts by using the average proportions of plagioclase and pyroxene. The glass volume fraction in the groundmass of each sample was used to correct for the highly variable quantity of microlites. Each correction was done with the maximum, minimum and average glass contents of that sample, yielding up to nine corrected glass water contents per sample, from which a median value and a standard deviation was calculated. Water in amphibole was neglected, as the small proportion of this mineral caused corrections well below measurement error.

2.4. Two-step decompression model

As shown later, the vesicularity of the samples has changed during the explosion such that the pre-explosive vesicularity must be reconstructed. With bulk measurements at hand and complex, heterogeneous pumice textures that preclude detailed modeling of the syn-

explosive evolution of our samples, we opt for a simple physical approach in two steps (Fig. 4). The first step describes the state of a magma parcel in the column just prior to explosion, and the second step characterizes this parcel at quench time, once explosion and individualization of each pumice clast has taken place. These steps hold true whether quenching occurs because of temperature drop (Kaminski and Jaupart, 1997) or viscosity increase due to water loss. We simply assume that clast individualization (i.e. magma fragmentation) occurs sometime between these two stages. In addition, we assume that the steps are isothermal, because the time for thermal equilibration of the clasts $[\approx (\pi d^2)/(4\kappa)$, with $\kappa = 10^{-6}$ m^2/s, $d = 1.6$ cm diameter for clasts analyzed by Clarke et al. (2007) and $d = 7$ cm for our samples] lies between 2 minutes and 7 hours and is greater than the travel time from conduit to deposition except for some dense samples. For simplicity, we use indifferently porosity or vesicularity when referring to the gas fraction. We left out of our analysis the interiors of the breadcrusted bombs because they were still expanding while their glassy rims were quenched in a state close to pre-explosive.

Prior to explosion, each future clast is located at pressure P_i, has a porosity α_i, and a water weight fraction distributed as exsolved, x_i, and dissolved, s_i (Fig. 4). Sometime during evacuation from the conduit, the clast is quenched at pressure P_q, porosity α_q, and dissolved water content, s_q. If all the vesicularity we measured in the pumices was acquired during the explosion solely by closed-system decompression of the pre-explosive gas, the weight fraction of gas at quenching would be equal to that at depth, x_i. Explosion duration, however, was not short enough to totally inhibit water diffusion and outgassing before quenching (Giachetti et al., accepted). We thus consider that the exsolved water content varies because water *1)* diffuses out of the melt as bubbles grow syn-explosively and *2)* escapes from clasts by outgassing (Fig. 4). In other words, the total exsolved water content is a combination of

gas trapped in the vesicles and gas expelled (outgassed) from the clast interior to its surroundings.

Giachetti et al. (accepted) noticed in pumices a distinct population made of small (< tens of μm) isolated vesicles, a population of slightly larger (< hundreds of μm) coalesced vesicles that are connected to the outside of the clasts, and a population of larger (hundreds of μm to a few mm) connected and deformed vesicles. They interpreted the two first populations as having nucleated, grown, and coalesced in a syn-explosive fashion, and the third one as having mostly a pre-explosive origin. We use the three bubble populations recognized by Giachetti et al. (accepted) to quantify these syn-explosive changes. The amount of water that diffused out of the melt to create the isolated vesicles identified by Giachetti et al. (accepted) is x_{d1}. It is not affected by outgassing. Connected, syn-explosive vesicles, on the other hand, have a total gas content, x_{d2}, of which outgassing leaves x_{q2} in the quenched clast. Outgassing also affects the pre-explosive gas content, x_i, of which only x_{q1} remains in the quenched clast as large, connected vesicles of pre-explosive origin. The total amount of gas lost by clasts, x_{out}, is thus composed of a syn-explosive part, x_{d2}-x_{q2}, and a pre-explosive part, x_i-x_{q1}, and the total gas content at quench time is composed of a pre-explosive component, x_i, and an exsolved component, x_{d1}+x_{d2}. Mass balance stipulates:

$$x_{out} = (x_i - x_{q1}) + (x_{d2} - x_{q2}) \tag{1}$$

We assume outgassing proportionally removes gas from connected vesicles of both syn- and pre-explosive types:

$$x_{q2}/x_{d2} = x_{q1}/x_i \tag{2}$$

Giachetti et al. (accepted) found that the relative proportions of pre- and syn-explosive vesicularities are broadly similar from clast to clast. We can thus define a global diffusion rule for our two-step model, by which the ratio between the amounts of gas in syn-eruptive and pre-explosive vesicles, E, remains constant for all samples:

$$E = \left(x_{d1} + x_{q2} \right) / x_{q1} \tag{3}$$

We define a similar, constant ratio between the amounts of gas in isolated syn-eruptive vesicles and pre-explosive vesicles, F:

$$F = x_{d1} / x_{q1} \tag{4}$$

There is no easy way, however, to quantify the variable x_{out} as clasts become permeable and travel through a medium of lesser pressure without assigning a temporal behavior to all variables between the pre-explosive stage and the quenched stage. Assuming that the observation of Giachetti et al. (accepted) can be extended to outgassing, we also use a constant ratio between outgassing and the amount of water unaffected by it, G:

$$G = x_{out} / x_{q1} \tag{5}$$

The KFT water content reported in Table 1 is relative to the amount of bubble-free glass, whereas all the quantities in our two-step model are relative to the total amount of melt plus bubbles. Ignoring the small density change between glass and melt, naming the bubble-free water content in Table 1 $wt_{H2O\,q}$, and naming the pre-explosive, bubble-free water content $wt_{H2O\,i}$, conversion can be carried out by:

$$s_q = wt_{H2O\,q}(1 - x_{d1} - x_{d2} - x_i) \tag{6}$$

$$s_i = wt_{H2O\,i}(1 - x_i) \tag{7}$$

Pre-explosive melt water content s_i differs from the quenched melt water content, s_q, because of syn-explosive exsolution:

$$s_q = s_i - x_{d1} - x_{d2} \tag{8}$$

For the purpose of our model, we use the solubility law of Liu et al. (2005) to relate P_i to the pre-explosive melt water content, $wt_{H2O\,i}$:

$$wt_{H2O\,i} = \frac{3.5494 \times 10^{-3} P_i^{0.5} + 9.623 \times 10^{-8} P_i - 1.5223 \times 10^{-11} P_i^{1.5}}{T} + 1.2439 \times 10^{-14} P_i^{1.5} \tag{9}$$

In general, clast porosity, α, is related to the mass fraction of the exsolved gas it contains, x, by mass balance:

$$\frac{1}{\alpha} = 1 + \frac{(1-x)\rho_g}{x\rho_m} \tag{10}$$

where ρ_m is the (constant) bubble-free magma density (~2450 kg/m^3 using Conflow, Mastin, 2002, and crystal + melt at 850 °C, Devine et al., 2003) and ρ_g is the gas density (kg/m^3), which is calculated according to the ideal gas law:

$$\rho_g = \frac{MP}{RT} \tag{11}$$

where P is the pressure (Pa), $M=0.018$ kg/mol is the molar weight of H_2O, $R=8.3144$ J/mol/K is the universal gas constant, and $T=1123$ °K is the (constant) gas temperature. To convert mass fraction to volume fraction at quench time, x in Eq. (10) must be replaced by $(x_{d1}+x_{q2}+x_{q1})/(1+x_{out})$ to correct for the outgassed fraction, yielding:

$$\frac{1}{x_{q1}} = G - (1+E)\left[1 + \frac{(1-\alpha_q)\rho_m}{\alpha_q\rho_g}\right] \tag{12}$$

Gas density in Eq. (12) depends on the quench pressure P_q, which lies between atmospheric pressure and the pressure at depth ($P_{atm}=0.1$ MPa $\leq P_q \leq P_i$). Values of P_q can be constrained between these two extremes by the fact that bubbles will only hold a modest amount of overpressure before breaking up and fragmenting the magma (Zhang, 1999). Experiments carried out on sample sizes similar to that of the clasts used in this study (e.g., Martel et al., 2001; Spieler et al., 2004; Mueller et al., 2008) suggest that vesicular clasts freshly erupted by the Vulcanian explosions are unable to withstand a pressure difference with the atmosphere of more than a few MPa. These studies applied very rapid decompression to magmas, on the order of GPa/s, and we believe such conditions are appropriate for Vulcanian clasts suddenly exposed to near atmospheric pressure. In particular, Mueller et al. (2008) have shown that this maximum overpressure can be related to the sample porosity and

permeability. By combining their relationship with a law converting permeability, k, into porosity, the maximum overpressure, $\Delta P_{Mueller}$, becomes a sole function of porosity. There are several laws relating permeability and porosity. We choose that of Klug and Cashmann (1996; $k=2\times10^{-12}\,\alpha^{3.5}$), although selecting, for instance, that of Costa (2006) gives nearly identical (<10%) overpressures:

$$\Delta P_{Mueller} = 1.161\times10^6\alpha_q^{0.75} + 1.54\times10^6\alpha_q^{-1} \tag{13}$$

Clasts we collected were not subjected to overpressure larger than $\Delta P_{Mueller}$. Many clasts of similar sizes, however, probably were, because the majority of ejecta are smaller than the clasts we collected. Since we cannot rely on firmer grounds to evaluate by how much P_q differs from $\Delta P_{Mueller}$, we simply introduce a linear parameter, H:

$$P_q = \min\left(P_i, P_{atm} + H\,\Delta P_{Mueller}\right) \tag{14}$$

The minimization ensures that clasts with a low pre-explosive pressure are considered to quench at that pressure.

We apply our model to two datasets: that of Table 1 and that of Clarke et al. (2007). Regardless of the dataset, the model requires that the four free parameters E, F, G, and H are constrained by independent observations. For our dataset, the goal is to evaluate the pre-explosive pressure, P_i, and porosity, α_i, using water content, $wt_{H2O\,q}$, and porosity, α_q, which represent the state of clasts at quench time. Once the values of the free parameters fixed, x_{q1} can be evaluated with Eq. (12) and the gas density at the quench pressure given by Eqs. (13-14). Some algebra yields simple expressions for the other variables as a function of x_{q1}, successively:

$$x_i = x_{q1}\left(1 + \frac{G}{1+E-F}\right) \tag{15}$$

$$s_q = \frac{wt_{H2Oq}}{1 - x_{q1}(1+G+E)} \tag{16}$$

$$s_i = s_q + Fx_{q1} + x_i(E - F) \tag{17}$$

Equations (7) and (9) can then be used to calculate pre-explosive pressures. The variable α_i is found by applying Eq. (10) with $\alpha = \alpha_i$ and $x = x_i$.

Pressures determined from feldspar microlite content (data from Clarke et al., 2007) directly correspond to P_i because explosion time is much shorter that microlite growth time. As with our samples, x_i can be found using Eqs. (12) and (15). The pre-explosive water content, s_i, can then be calculated from Eqs. (7) and (9).

3. Results

3.1. Clast textures

The most significant textural characteristics of the 1997 Vulcanian products are listed in Table 1 and illustrated in Fig. 2 and 3. Textures cover the recognized range of collected Vulcanian lithologies. All samples show the same phenocryst assemblage: plagioclase, amphibole, orthopyroxene, clinopyroxene and titano-magnetite. The phenocryst content on a bubble-free basis is similar in all lithologies. The densest lithology consists of dark glassy clasts (Fig. 2A) with vesicularities <10 vol%, and very microlite-rich (up to 51 vol%, Fig. 3A). Interstitial glass proportions (as a percentage of total solid volume) range from 40 to 53 vol%.

Homogeneous pumices are generally rounded to subequant, with colors varying from light grey to (less commonly) dark brown (Fig. 2B). Vesicularities range widely from 25 to 69 vol%. Vesicles are generally rounded with sizes varying from less than 1 μm to several mm. Interstitial glass proportions range from 40 to 63 vol%. Most plagioclase microlites are tabular with euhedral shapes (Fig. 3B).

Several types of texturally heterogeneous pumices have been recognized. Some clasts show linear banding with sharp limits at the macroscopic scale. Banding consists of dense parts with tabular shapes that form cm-thick streaks in a more vesicular clast (Fig. 2C). Often, dense bands display discrete zones with heavily coalesced bubbles forming oblong, cm-size cracks. These cracks are mostly perpendicular to the bands, although parallel cracks sometime occur (Fig. 2C). Other clasts show lobate to crenulate boundaries between the dense and vesicular parts (Fig. 2D). The textural heterogeneities we focused on herein are caused by changes in vesicularity rather than in crystallinity (Fig. 3C-D). Overall, vesicular parts (38 to 51 vol%) and dense parts (<5 to 29 vol%) have 26 to 52 vol% glass. There are no clear porosity or crystallinity differences between the vesicular parts of these clasts and pumices belonging to the homogeneous category.

Breadcrusted bombs are characterized by dark vitreous crusts surrounding light-grey interiors (Fig. 2E). Crust thicknesses vary from 5 mm to 2 cm with vesicularities of ≤6 vol%, whereas core vesicularities range from 8 vol% to 54 vol%. SEM observations of the groundmass showed no significant differences between the crust and the core in terms of crystallinities and microlite shapes and abundances (Fig. 3F), yielding glass contents ranging from 30 to 58 vol%.

Homogeneous pumices from fallout deposits are generally tabular with angular edges and curviplanar faces (Fig. 2F, Druitt et al., 2002). Their sizes range from 0.5 to 5 cm. Sizes and shapes of bubbles and microlites are more uniform than those of their counterparts found in pyroclastic flow deposits (Fig. 3B,E). Their vesicularities are also higher, ranging from 55 to 68 vol%, but it might simply reflect a sampling artifact. Interstitial glass proportions cluster between 30 and 38 vol%, which is probably due to their lower microlite content (<19 vol% of the groundmass).

Other studies on the 1997 products have defined clast classifications similar to the present one. Giachetti et al. (accepted) carried out a detailed study of bubble size distributions of the 1997 ejecta. It is based on the same sample suite as herein, including the five textural groups defined above. Kennedy et al. (2005) distinguished two types of Vulcanian pyroclasts according to porosities and textural features. Type 1 consists of high-porosity (60-68 vol%) samples with homogeneous textures, which correspond in our classification to fallout pumices and the most vesicular pumices from flow deposits. Type 2 consists of banded and brecciated samples with a large range of porosity (3-45 vol%), which corresponds broadly to our heterogeneous lithology. Clarke et al. (2007) have identified three main clast types based on porosities and plagioclase microlite morphologies and proportions. The first type comprises highly crystalline dense clasts equivalent to our dense lithology. The second type comprises highly vesicular pumices with moderately crystalline groundmasses, and the last type includes less vesicular pumices with moderately to weakly crystalline groundmasses. These types correspond broadly to our fallout and pyroclastic flow pumices, respectively.

3.2. Interstitial glass water content

Thirty-eight samples sorted by lithology were analyzed using Karl-Fischer Titration to quantify the pre-explosive water dissolved in the melt (Table 1). Figure 5 indicates that interstitial glass water content and lithology are correlated. Dense clasts have the lowest water contents, between 0.20 and 0.37 wt%. Homogeneous pyroclastic flow pumices have higher water contents, between 0.45 and 2.19 wt% with a mean value close to 1 wt%. Fallout pumices have even higher water contents, between 1.35 and 2.79 wt% with a mean value close to 2 wt%. Heterogeneous flow pumices have interstitial glass water contents that mirror the textural heterogeneity. The vesicular parts have water contents identical to those of

homogeneous pumices from flows deposits (close to 1 wt%), but the dense parts have

generally lower water contents, close to 0.5 wt%. When considering individual clasts, the

dense part also has systematically lower water content than the vesicular part. Such a

distinction cannot be drawn from measurements of the crusts and the cores of breadcrusted

bombs because error margins mostly overlap, yielding similar values close to 1 wt%.

3.3. Pre-explosive H_2O content and pressure estimates

Measured H_2O contents of the interstitial glasses can be converted into quench

pressure by the means of a solubility law adapted to low pressures, such as that of Liu et al.

(2005). The melt compositions used to establish this law are, however, more alkali-rich than

our interstitial glasses. We conducted solubility experiments (see Appendix A) that show that

these compositional effects can be neglected; the law of Liu et al. (2005) is applicable to

Soufrière Hills glasses. After each Vulcanian explosion, magma ascent speed exceeded ~2

cm/s (Druitt et al., 2002), which is slow enough to allow near-equilibrium degassing

(Burgisser and Gardner, 2005), as required to apply the solubility law. At the highest pressure

we consider, ~80 MPa, one can dissolve 3.43 wt% H_2O if CO_2 is not present. Calculations

carried out with the multicomponent solubility model of Burgisser et al. (2008) indicate that

the maximum CO_2 amount in the gas in ~4 mol%, which, if taken in account in the solubility

law, lowers these 3.43 wt% H_2O by 0.08 wt%. This is below analytical error and drives us to

neglect the possible contribution of CO_2. We mostly considered silica precipitate as glass,

thus underestimating glass water contents. The occurrence of such precipitate during the

crystallization of silica-rich melts is poorly known (Martel and Poussineau, 2007), and

correcting for its influence on the vapor-liquid partition at depth is beyond the scope of this

work. Assuming for now that little H_2O exsolution took place on the timescale of explosion

(e.g., Melnik and Sparks, 2002) allows us to use the H_2O content in the glasses to calculate

quench pressures (Table 1). This last assumption will be evaluated in the next section.

An independent method to retrieve pre-explosive pressures of the 1997 Vulcanian

clasts has been used by Clarke et al. (2007). It is based on the power-law relationship between

feldspars microlite volume proportion in groundmass and experimental multi-steps

decompression data on microlite crystallization (Hammer and Rutherford, 2002; Couch et al.,

2003). We applied to our samples the procedure described in Clarke et al. (2007) to retrieve

feldspar microlite contents (Table 1) and calculate pre-explosion pressures. Results show a

broad agreement between pressures calculated this way and those calculated by glass H_2O

contents (Fig. 6). The comparison of error estimates for each method shows that pressure

calculation from microlite content is more accurate at low pressure (<10 MPa) because of the

high crystallization rate at low pressure, whereas at high pressure (>10 MPa), the method

using glass H_2O can be more precise because of low groundmass crystallinities. In what

follows, we add the microlite-derived pressures from the 23 samples analyzed by Clarke et al.

(2007) to our H_2O-derived pressures (Table 1).

3.4. Magma column density evaluation and pre-explosive pressure estimates

Reconstruction of the conduit stratigraphy implies converting clast vesicularities into

pre-explosive porosities. When quench pressures are thought to equal those at depth ($P_q=P_i$),

as commonly assumed (Formenti et al., 2003; Clarke et al., 2007; Diller et al., 2006), the pre-

explosive porosity profile increases with depth up to values of 68 vol% (Fig. 7A). Such large

porosities at depth correspond to a significant amount of water, to which must be added the

large amounts of dissolved water still present in most clasts (Table 1). Was there enough

water in the reservoir to account for both dissolved and exsolved water? There are three lines of evidence that it is not the case.

Experimental petrology results suggest that the chamber beneath Soufrière Hills lies at about 130 MPa (Barclay et al., 1998; Rutherford and Devine, 2003), which yields 4.6 wt% H_2O using the solubility law of Liu et al. (2005). Assuming slow, isothermal magma column emplacement, the maximum porosity distribution as a function of decreasing pressure is given by the equilibrium exsolution law applied to a closed system for this initial water content (e.g., Jaupart and Allègre, 1991). In Fig. 7A, the region bounded by the thick continuous line covers porosities that can be achieved in the conduit with 4.6 wt% H_2O in the reservoir. The presence of a free gas phase in the reservoir cannot be excluded at Montserrat. As an illustration, the thin continuous line shows that a reservoir with 2 wt% gas is not enough to explain the porosities at depth. At least 10.6 wt% total H_2O is needed to reach 68 vol% porosity at 49 MPa, well above the high end of the values commonly reported in arc volcanoes (Wallace, 2005).

Most of the energy available for pyroclast evacuation during a Vulcanian explosion comes from the compressed gas (Woods, 1995; Formenti et al., 2003). Equations (10-11) with $P=P_i$ can be used to convert mass fraction to volume fraction. If the quench vesicularity is equal to that at depth, the amount of available gas just before explosion, x, is well above that determined by detailed analysis of video footage of the first seconds of the explosions (Formenti et al., 2003): up to 8 wt% at 49 MPa whereas less than 2 wt% are needed for the propulsion of the Vulcanian jets (Fig. 7B). In other words, the jets should have reached exit velocities much larger than those observed.

Giachetti et al. (accepted) recognized in pumices three vesicle populations, one only being pre-explosive. It is thus clear that, between their individualization as fragments and their final quenching, pumices undergo changes in porosity as volatiles trapped in the melt

exsolve, and as the gas expands, possibly escaping through heavily coalesced vesicles. As a result, the porosity of a pumice collected in the field does not correspond to that at depth, despite the short duration of a Vulcanian explosion. Below we use the two step degassing model developed in section 2.4 to quantify these syn-explosive changes.

3.5. Constraints on the four free parameters of the model

Our simple physical model depends on four free parameters: E, F, G, and H (Fig. 4). Parameters E and F, which quantify syn-explosive degassing, can be tightly constrained by the textural observations of Giachetti et al. (accepted), which establish that vesicles are either isolated syn-explosive (x_{d1}), or connected syn-explosive (x_{q2}), or connected pre-explosive (x_{q1}). Vesicles occur in the respective proportions of 16:50:34, which yields $E=1.9$ and $F=0.5$. We framed these values by either ignoring breadcrust rims in the averaging so as to maximize syn-explosive degassing (11:69:20, $E=4.1$, and $F=0.6$), or considering that only isolated vesicles were produced by it (16:0:84, $E=0.2$, and $F=0.2$). The former extreme values mean that 80% of the vesicularity is syn-explosive, which approaches the case of breadcrust bombs.

The minimum amount of gas available for propulsion of the Vulcanian jets is the pre-explosive gas content, x_i, and the maximum amount is $x_{d1}+x_{d2}+x_i$. Because the latter sum can be expressed as $x_{q1}(1+E+G)$, the value of the parameter G, which quantifies outgassing, strongly controls the amount of propelling gas. Thus, for each E value, we choose G such that the span of maximum exsolved gas values lies within that measured by Formenti et al. (2003). There are two other independent maximum values for G, given by $x_i+s_i \leq 4.6$ wt% H_2O and $x_{d1}+x_{d2} \leq s_i$. The former condition ensures that there was no more water present in the conduit than was available in the reservoir; it can only be evaluated for our samples and it is always fulfilled. The latter condition stipulates that there should not be more water exsolved syn-

19

explosively than was available in the melt and it is very sensitive to the value of quench porosity. It is fulfilled for every sample but the most vesicular samples analyzed by Clarke et al. (2007), for which it causes negative values for s_q. For these samples, reducing vesicularities from ~75 to ~65 vol% would be sufficient to avoid this discrepancy. Such reduction being comparable to the analytical error on vesicularities, we decided that strict enforcement of this condition was not necessary and accepted G values such that no more than 4 of the 23 vesicular samples yielded negative s_q values.

There is a maximum value for the parameter that fixes quench pressures, H, because the maximum amount of propelling gas is controlled by x_{q1} and thus P_q (see above). If G is set to 0, H can reach at most 2.2 before the gas content exceeds that needed to propel the Vulcanian jets. We thus tested values of quench pressures from P_{atm} to that maximum, varying H between 0 and 2.2.

3.6. Pre-explosive state of the magma column

We varied the values of the four free parameters between the respective bounds established above. To select the most likely parameter set, we used *1)* the ratio between the water outgassed and that trapped in the connected vesicles at quench time, $x_{out}/(x_{q1}+x_{q2})$, and *2)* the ratio between pre-explosive and quench porosity, α_i/α_q.

For each parameter set, there is only one value for the ratio between the water outgassed and trapped in connected vesicles, $x_{out}/(x_{q1}+x_{q2})$. Giachetti et al. (accepted) showed that syn-eruptive vesicles are generally larger when connected than when isolated because coalescence created the connected vesicles from the isolated ones. Outgassing, on the other hand, works the opposite way because it can reduce the size of connected vesicles by collapse but does not affect isolated ones. Outgassing was not a dominant process because isolated

20

vesicles have not grown larger than connected vesicles subjected to outgassing. This suggests that $x_{out}/(x_{q1}+x_{q2})$ is not $\gg 1$.

The ratio α_i/α_q indicates whether clasts had an overall inflation or deflation during the explosion. The large, deformed and coalesced vesicles in the ejecta that likely pre-date the explosion represent ~34% of the vesicle volume fraction (Giachetti et al., accepted). Such textures can indifferently be attributed to pre- or syn-explosive deflation. The dominant syn-eruptive vesicles, however, display evidences of net inflation. Many fallout pumices also suggest net inflation because their angular shapes have clearly been bloated. The ratio α_i/α_q can thus be expected to lie below unity.

Figure 8 shows the two ratios for 10 representative sets of free parameters. The choice of quench pressure through the factor H is the strongest control on the amount of outgassing, whereas the amount of syn-eruptive degassing has a modest influence. Using the criteria developed above $[x_{out}/(x_{q1}+x_{q2}) \le 1, \alpha_i/\alpha_q \le 1]$, scenarios with $H \ge 1$ are the most realistic. We took the conservative approach to use an intermediate parameter set as the most representative: $H=1$, $G=2.7$, and the average degassing constants $E=1.9$ and $F=0.5$. Such parameters yield a ratio $x_{out}/(x_{q1}+x_{q2})$ of ~0.9, which means that about 47% of the gas trapped in the connected vesicles at quench escaped syn-explosively, and that clasts were quenched, on average, at the maximum overpressure that they could sustain. Figure 9 illustrates the resulting pre-explosive pressure and porosities and we report in Table 2 salient model outputs. We show the span of values created by the two extreme parameter sets as a gray area. The denser limit of the gray area is given by the sets maximizing syn-explosive degassing ($E=4.1$ and $F=0.6$), whereas the less dense limit is given by the sets minimizing syn-explosive degassing ($E=0.2$ and $F=0.2$). Errors bars on Fig. 9 represent outputs values for the typical set using the analytical uncertainties on glass water content and vesicularity (Table 1). In general, Fig. 9 shows that error propagation maintains a distinct P-shaped porosity profile. This shape

is robust, as the envelope due to the range of values of the four free parameters closely matches that due to measurement errors. The relationship between pressure and lithology noted in Fig. 5 also exists pre-explosively; the conduit has a shallow dense region followed by a deeper heterogeneous zone with large porosity variations at pressures <10 MPa and low, slowly decreasing porosities at higher pressures that reach near-closed degassing conditions at the deepest sampled level (~80 MPa). Overall, the column is denser than if it was emplaced under closed-system degassing. This also is a robust result because unrealistic values would need to be imposed on the free parameters in order to move the trend across to closed-system degassing.

The pre-explosive gas content distribution, from which derives most of the energy sustaining the Vulcanian column, is shown in Fig. 10 for the typical set of free parameters. By design, it is within the range determined by detailed analysis of video footage of the first seconds of the explosions (Formenti et al., 2003). Interestingly, the amount of gas of the deeper homogeneous region is nearly constant around 1 wt%.

We showed that the pre-explosive pressures derived from microlite content are broadly comparable to those derived from water content (Fig. 6). It remains true when the water-derived pressures are calculated by our model; the model uncertainties are on the same order as those caused by the analysis of water content. This broad agreement should, however, be tested more precisely because the presence of a significant amount of syn-explosive degassing implies that it could be inaccurate to estimate pre-explosive pressures using glass water content only, such as in Table 1 and Fig. 6. Figure 11 shows that the amount of correction on pressure introduced by syn-explosive degassing is well above error and nearly linear; model-derived pressures are roughly 1.5 times above those derived from glass water content. Thus, both corrections on pressure and porosity (α_i/α_q from 0.1 to 0.9, Fig. 8) are significant and impact the state of the magmatic column just prior to a Vulcanian event.

4. Discussion

The average pre-explosive magmatic column is denser than if it was emplaced under closed system degassing. This could be the result of a fast emplacement under closed system degassing and subsequent collapse back to a denser column, or emplacement under partly open system degassing. We favor the latter scenario because the transition between closed and open degassing occurs over minutes (Burgisser and Gardner, 2005), well below column emplacement time. Our vision of the pre-explosive column is composed of three main parts as illustrated in Fig. 9. The shallower part is composed by a highly degassed plug of magma. This dense plug is probably highly fractured because of its intrinsic properties (high crystallinity and very low water content of the residual melt). The degassed plug is overlain by a transition zone characterized by complex mingling between vesicular and dense magma. This level is well-constrained by pressures ranging from 1 to 10 MPa, which is consistent with the critical level at ~7 MPa identified by Clarke et al. (2007), where system permeability and crystal nucleation are significantly enhanced. Our model still marks a pre-explosive vesicularity difference between dense and vesicular parts of heterogeneous pumices (Table 2). This is more the result of our first-order approach fixing the proportion of syn-explosive degassing and outgassing to single values for all samples than reflecting pre-explosive heterogeneity. Nevertheless, taking into account the uncertainties in pressure, these samples reflect local pre-explosive heterogeneities in melt water content. Kennedy et al. (2005) have proposed a conceptual model for 1997 Vulcanian explosions based on textural observations and fragmentation speed experiments. In their model, variations in clast density are explained by strong horizontal gradients within the pre-explosive column, which would be dense at conduit walls and porous at the center. On the other hand, the groundmass-crystallinity based study of Clarke et al. (2007) suggests that the pre-explosive column would bear essentially

23

vertical variations of porosity. As suggested by Lane et al. (2008), these two views are not necessarily opposed. While a general vertical stratification in porosity is unavoidable (Fig. 9), the strong overlap of samples in the heterogeneous transition zone suggests that stratification might not be exclusively vertical. Although the pre-explosive vesicularities in the transition zone given by our model are maximum estimates because most of these samples were located at pressures lower than $\Delta P_{Mueller}$, our data show that this zone displays strong porosity variations that can easily be explained by horizontal heterogeneities. We found no evidence supporting whether the exterior of the column was consistently denser than the inside, as we never observed dense clasts with high water content nor found any textural evidence of strongly sheared products. Instead, we simply favor a heterogeneous transitional zone where particularly uneven amounts of compressed gas were available for jet propulsion (Fig. 10).

This heterogeneity of the exsolved gas within the magmatic conduit at shallow depth has implications on the dynamics of the Vulcanian explosions. Detailed analysis of video footage of the first seconds of the explosions showed that they were formed of multiple jets 2-12 m in diameter at initiation (Formenti et al., 2003). This pulsatory behavior suggests textural and water content heterogeneities promote piecemeal fragmentation of the column.

Our data support the existence of shallow vesicular parts reaching values (50-60 vol%) close to where various fragmentation mechanisms are thought to operate most efficiently (Gardner et al., 1996; Spieler et al., 2004). These values are consistent with estimates based on textural observations, such as amphibole boudinage (Giachetti et al., accepted). This opens the possibility that the presence of such large vesicularities in the transition zone controls whether the eruption unfolds as a Vulcanian explosion rather than a dome-forming effusion. Establishing the relationship between such high-porosity zones and the development of column pressurization might thus be essential to determine the trigger mechanism(s) of Vulcanian dynamics. This is the subject of a companion paper (Burgisser et al., submitted).

Beneath the transition zone, we identified a much more homogeneous zone of relatively dense (10-20 vol%) magma. All homogeneous pumices from fallout issued from this deeper zone, which thus fed the most buoyant parts of the Vulcanian column. The vesicularity distribution of this zone implies that the magma column evacuated by the explosions was emplaced under partly open system degassing. We speculate that the numerous large, deformed and coalesced bubbles that pre-date the explosion (Giachetti et al., accepted) are witnesses of the partial collapse of the freshly emplaced column.

Does fragmentation occur early in the explosion, when magma is close to P_i, or after a progressive decompression until a value close to P_q? In the former case, the whole column fragments nearly in situ and clasts continue their individual decompression until quenching. In the latter case, we expect the column to expand in a coherent way before fragmenting because of decompression-induced bubble nucleation and growth. Figure 12 shows the starting pressure (P_i) and the quench pressure (P_q) for all samples. It also shows the respective span of maximum instant overpressure samples could have sustained pre-explosively (i.e. at α_i using the laws by Mueller et al., 2008, and Spieler et al., 2004). As expected, maximum overpressures are above those of confinement in the upper part of the pre-explosive column, from the dense cap to the transitional heterogeneous zone. More surprising are the large values of overpressure (~30 MPa) necessary to disrupt this upper part and have the possibility to initiate a Vulcanian explosion. Immediately below, a sudden decompression of only 3.5 MPa, on average, is necessary to fragment the homogeneous zone. This remarkably small value reinforces the image of a highly unstable magma column overlain by a very strong veneer cap. At depth, clasts have expanded by more than 50% syn-explosively ($\alpha_i < \alpha_q$, Tables 1-2), whereas in the shallowest part of the homogeneous zone pre- and post-explosive vesicularities are much more similar. One clast issued from this shallow part (R2, 11 MPa from 16.8 vol% plagioclase microlite, analyzed by Giachetti et al., accepted) displays a

distinctive curviplanar, tabular shape. Such shapes are characteristic of homogeneous fallout

pumices, and have been suggested to be inherited from magma spallation (Druitt et al., 2002).

This and the absence of vesicularity gradient in these pumices (Giachetti et al., accepted)

imply limited post-fragmentation expansion of the shallow homogeneous zone. These various

lines of evidence support alternatively both end-member scenarios and we are inclined to

conclude that some column-wide expansion occurred before fragmentation, followed by

column-wide fragmentation. As a result, clasts were individualized close to P_i in the shallow

part, and deeper magma decompressed somewhat before fragmentation.

It is most likely that clasts quenched at pressures well above atmospheric (Fig. 8), and

our two-step decompression model suggests most of them quenched around the maximum

overpressure they could sustain (H=1). The relationship we used to derive maximum

overpressure takes in account clast permeability, which allowed a significant fraction of gas

[$x_{out}/(x_{q1}+x_{q2})$~0.9] to escape at or just prior to quenching. It is thus likely that despite their

permeability, many clasts underwent secondary fragmentation in the column as a result of

overpressure.

In summary, fragmentation likely occurred in stages: it evacuated the transition zone

in a piecemeal fashion, but it could have affected the entire column below at once. Another

fragmentation stage probably occurred again at (or shortly after) quenching. Despite their

short duration, Vulcanian explosions involve a rather complex sequence of magma

fragmentation. Our analysis suggests that the amount and the degree of heterogeneity of

degassing occurring in the column are key controls of the likelihood and style of

fragmentation.

5. Conclusions

We determined interstitial glass H_2O contents and textural features of typical clasts erupted during a series of 88 Vulcanian explosions that occurred in August-September 1997 at Soufrière Hills volcano (Montserrat Island). Textural observations allowed us to identify five lithologies of Vulcanian products (glassy to crystalline dense clasts, breadcrusted bombs, texturally heterogeneous pumices, texturally homogeneous pumices, and homogeneous pumices from fallout deposits). Interstitial glass water contents were used to constrain confinement pressures prior to explosion. Analysis of these data demonstrated a clear relationship between lithology and pre-explosive storage pressure. Our results compare well with pre-explosive pressures of the same eruptive sequence based on groundmass crystallinities (Clarke et al., 2007), which allowed us to consider the two datasets together to reconstruct an average pre-explosive state of the magma column.

We developed a two-stage degassing model that links pre-explosive pressure and water content to those at quenching and takes into account gas expansion by decompression, water exsolution, and outgassing from clast interiors to their surroundings. It showed that syn-explosive degassing affects greatly the way porosity evolves by decompression during an explosion. This leads us to propose a pre-explosive porosity distribution with overall denser values than those previously suggested. This P-shaped distribution features a highly degassed plug of magma at the shallowest pressures, immediately followed by a transition zone composed of an intimate mingling between vesicular and dense magma. These two levels are well-constrained by pressures ranging from 1 to 10 MPa, and define a shallow vesicular zone reaching up to 70 vol%. Beneath lies a much more homogeneous zone of relatively dense (10-20 vol%) magma that extends to ~80 MPa. The porosity distribution of this zone implies that the magma column evacuated by the explosions was emplaced under partly open system degassing.

This conduit stratigraphy gives the vision of a strongly heterogeneous magma column immediately prior to its disruption. Our analysis suggests that fragmenting such a composite magma cannot happen in a single coherent pulse, but rather as stages. The heterogeneous transition zone probably fragmented in a piecemeal fashion, whereas the much more homogeneous column below could have fragmented at once. Part of the clasts underwent another fragmentation stage in the jet, at or shortly after quenching.

Acknowledgments

Appendix A: Water solubility experiments

Water solubility experiments were performed on a rhyolitic composition, VH, that corresponds to an average composition of the interstitial glass in 1997 Vulcanian pumices (Table A1). VH glasses were prepared from a mixture of oxides (SiO_2, Al_2O_3, TiO_2, FeO, MgO and MnO) and carbonates (Na_2CO_3, $CaCO_3$ and K_2CO_3). All carbonates were heated at about 700°C to evacuate the maximum of CO_2. The mixture obtained was finely crushed and fused at 1 atm and 1400°C in a Pt crucible for 3 hours under oxidizing conditions. The glasses

were then crushed again and subjected to a second fusion. Electron microprobe analyses were performed on each chip of glass to check the chemical and textural homogeneity. Cylinders from these chips and an amount of water sufficient to ensure over-saturated conditions were fitted in 2.5-mm-diameter gold tubes with one welded end. The other end of the tube was welded while the capsule was cooled by external water to prevent water loss during welding. This was checked by weighing the capsule before and after sealing. Solubility experiments were performed during 6-7 days in an internally heated pressure vessel (Mo-wired IHPV, Basset type) under oxidizing condition (ΔNNO+3) with Ar as pressure medium. Capsules were placed into the hot zone of the furnace monitored by 3 thermocouples, so that the temperature gradient never exceeded 5°. Experiments were terminated by isobaric quench to prevent bubble nucleation during the ~100 °C/min cooling. Capsules were pierced and dried at 120°C before Karl-Fischer titration of the glass water content (3 measurements per charge). As illustrated in Fig. A1, the law of Liu et al. (2005) is in good agreement with our experimental melt H_2O contents.

References

Barclay, J., Rutherford, M.J., Carroll, M.R., Murphy, M.D., Devine, J.D., Gardner, J.E., Sparks, R.S.J., 1998. Experimental phase equilibria constraints on pre-eruptive storage conditions of the Soufriere Hills magma. Geophys. Res. Lett. 25, 3437-3440.

Behrens, H., Romano, C., Nowak, M., Holtz, F., Dingwell, D., 1996. Near-infrared spectroscopic determination of water species in glasses of the system $mAlSi_3O_8$ (m=Li, Na, K): an interlaboratory study. Chem. Geol. 128, 41-63.

Burgisser, A., Gardner, J.E. 2005. Experimental constraints on degassing and permeability in volcanic conduit flow. Bull. Volcanol. 67, 42-56.

Burgisser, A., Scaillet, B., Harshvardhan, 2008. Chemical patterns of erupting silicic magmas and their influence on the amount of degassing during ascent. J. Geophys. Res. 113, B12204, doi:10.1029/2008JB005680

Burgisser, A., Arbaret, L., Druitt, T.H., Giachetti, T., (submitted) Pre-explosive conduit conditions of the 1997 Vulcanian explosions at Soufrière Hills Volcano, Montserrat: II. Depth and overpressure distribution, J. Volcanol. Geotherm. Res.

Clarke, A.B., Neri, A., Voight, B., Macedonio, G., Druitt, T.H., 2002. Computational modelling of the transient dynamics of the August 1997 Vulcanian explosions at Soufriere Hills Volcano, Montserrat: influence of initial conduit conditions on near-vent pyroclastic dispersal. In: Druitt, T.H., Kokelaar, B.P. (Eds.) The eruption of Soufrière Hills Volcano, Montserrat, from 1995 to 1999. Geological Society of London Memoir, 21, 319-348.

Clarke, A.B., Stephens, S., Teasdale, R., Sparks, R.S.J., Diller, K., 2007. Petrologic constraints on the decompression history of magma prior to vulcanian explosions at the Soufrière Hills Volcano, Montserrat. J. Volcanol. Geotherm. Res. 161, 261-274.

Costa, A., 2006. Permeability-porosity relationship: a re-examination of the Kozeny-Carman equation based on fractal pore-space geometry. Geophys. Res. Lett. 33, L02318, doi:10.1029/2005GL025134.

Couch, S., Sparks, R.S.J., Carroll, M.R., 2003. The kinetics of degassing-induced crystallization at Soufriere Hills Volcano, Montserrat. J. Petrol. 44, 1477-1502.

Devine, J.D., Rutherford, M.J., Norton, G.E., Young, S.R., 2003. Magma storage region processes inferred from geochemistry of Fe-Ti oxides in andesitic magma, Soufrière Hills volcano, Montserrat, W.I. J. Petrol. 44, 1375-1400.

Diller, K., Clarke, A.B., Voight, B., Neri, A., 2006. Mechanisms of conduit plug formation: Implications for vulcanian explosions. Geophys. Res. Lett. 33, doi:10.1029/2006GL027391

Druitt, T.H., Young, S.R., Baptie, B.J., Bonadonna, C., Calder, E.S., Clarke, A.B., Cole, P.D., Harford, C.L., Herd, R.A., Lockett, R., Ryan, G., Voight, B., 2002. Episodes of cyclic Vulcanian explosive activity with fountain collapse at Soufrière Hills Volcano, Montserrat. In: Druitt, T.H., Kokelaar, B.P. (Eds.) The eruption of Soufrière Hills Volcano, Montserrat, from 1995 to 1999. Geological Society of London Memoir, 21, 281-306.

Eichelberger, J., Carrigan, C., Westrich, H., Price, R., 1986. Non-explosive silicic volcanism. Nature 323, 598-602.

Formenti, Y., Druitt, T.H., 2003. Vesicle connectivity in pyroclasts and implications for the fluidisation of fountain-collapse pyroclastic flows, Montserrat (West Indies). Earth Planet. Sci. Lett. 214, 561-574.

Formenti, Y., Druitt, T.H., Kelfoun, K., 2003. Characterisation of the 1997 Vulcanian explosions of Soufrière Hills Volcano, Montserrat, by video analysis. Bull. Volcanol. 8, 587-605.

Gardner, J.E., Thomas, R.M.E., Jaupart, C., Tait, S., 1996. Fragmentation of magma during Plinian volcanic eruptions. Bull. Volcanol. 58, 144-162.

Giachetti, T., Druitt, T.H., Burgisser, A., Arbaret, L., Galven, C. (accepted) Bubble nucleation, growth and coalescence during the 1997 Vulcanian explosions of Soufrière Hills Volcano, Montserrat. J. Volcanol. Geotherm. Res.

Hammer, J.E., Rutherford, M.J., 2002. An experimental study of the kinetics of decompression-induced crystallization in silicic melt. J. Geophys. Res. 107, 1-24.

Harford, C., Sparks, R., Fallick, A., 2003. Degassing at the Soufrière Hills Volcano, Montserrat, recorded in interstitial glass compositions. J. Petrol. 44, 1503-1523.

Holtz, F., Behrens, H., Dingwell, D.B.,Taylor, R.P., 1992. Water solubility in aluminosilicate melts of haplogranite composition at 2 Kbar. Chem. Geol. 96, 289-302.

Holtz, F., Behrens, H., Dingwell, D., Johannes, W., 1995. H_2O solubility in haplogranitic melts: compositional, pressure, and temperature dependence. Am. Mineral. 80, 94-108.

Jaupart, C., Allègre, C.J., 1991. Gas content, eruption rate and instabilities of eruption regime in silicic volcanoes. Earth Planet. Sci. Lett. 102, 413-429.

Kaminski, E., Jaupart, C., 1997. Expansion and quenching of vesicular magma fragments in Plinian eruption. J. Geophys. Res. 102, 12187-12203.

Keating, G.N., Valentine, G.A., Krier, D.J., Perry, F.V., 2007, Shallow plumbing systems for small-volume basaltic volcanoes. Bull. Volcanol. 70, 563-582.

Kennedy, B., Spieler, O., Scheu, B., Kueppers, U., Taddeucci, J., Dingwell, D.B., 2005. Conduit implosion during vulcanian eruptions. Geology 33 (7), 581-584.

Klug, C., Cashman, K.V., 1996. Permeability development in vesiculating magmas: implications for fragmentation. Bull. Volcanol. 58, 87-100.

Lane, S.J., Phillips, J.C., Ryan, G.A., 2008. Dome-building eruptions: insights from analogue experiments. In: Lane, S.J., Gilbert, J.S. (Eds.) Fluid motions in volcanic conduits: a source of seismic and acoustic signals. Geological Society of London Special Publication 307, 207-237.

Liu, Y., Zhang, Y., Behrens, H., 2005. Solubility of H_2O in rhyolitic melts at low pressures and a new empirical model for mixed $H_2O – CO_2$ solubility in rhyolitic melts. J. Volcanol. Geotherm. Res. 143, 219-235.

Martel, C., Dingwell, D.B., Spieler, O., Pichavant, M., Wilke, M., 2001. Experimental fragmentation of crystal- and vesicle-bearing silicic melts. Bull. Volcanol. 63, 398-405.

Martel, C., Poussineau, S., 2007. Diversity of eruptive styles inferred from the microlites of Mt Pelée andesite (Martinique, Lesser Antilles). J. Volcanol. Geotherm. Res. 166, 233-254.

Mastin, L.G. (2002) Insights into volcanic conduit flow from an open-source numerical model. Geochem. Geophys. Geosyst. 3. doi:10.1029/2001GC000192.

Morrissey, M.M., Mastin, L.G., 2000. Vulcanian eruptions. In: Sigurdsson (Ed.) Encyclopedia of Volcanoes. Academic Press, San Diego, 463-475.

Mueller, S., Scheu, B., Spieler, O., Dingwell, D.B., 2008. Permeability control on magma fragmentation, Geology 36, 399-402.

Rutherford, M.J., Devine, J.D., 2003. Magmatic conditions and magma ascent indicated by hornblende phase equilibria and reaction in the 1995-2002 Soufrière Hills magma. J. Petrol. 44, 1433-1454.

Self, S., Wilson, L., Nairn, I.A., 1979. Vulcanian eruption mechanisms. Nature 277, 440-443.

Spieler, O., Kennedy, B., Kueppers, U., Dingwell, D.B., Scheu, B., Taddeucci, J., 2004. The fragmentation threshold of pyroclastic rocks. Earth Planet. Sci. Lett. 226, 139-148.

Stasiuk, M.V., Barclay, J., Carroll, M.R., Jaupart, C., Ratte, J.C., Sparks, R.S.J., Tait, S.R., 1996. Degassing during magma ascent in the Mule Creek vent (USA). Bull. Volcanol. 58, 117-130.

Stix, J., Torres, R.C., Narvaez M, L., Cortes J, G.P., Raigosa, J.A., Gomez M, D., Castonguay, R., 1997. A model of Vulcanian eruptions at Galeras Volcano, Colombia. J. Volcanol. Geotherm. Res. 77, 285-303.

Turek, A, Riddle, C., Cozens, B.J., Tetley, N.W. 1976. Determination of chemical water in rock analysis by Karl Fischer titration. Chem. Geol. 17, 261-267.

Wallace, P.J., 2005. Volatiles in subduction zone magmas: concentrations and fluxes based on melt inclusions and volcanic gas data. J. Volcanol. Geotherm. Res. 140, 217-240.

Westrich, H.R., 1987. Determination of water in volcanic glasses by Karl-Fischer Titration. Chem. Geol. 63, 335-340.

Woods, A.W., 1995. A model of vulcanian explosions. Nuclear Engin. Design. 155, 345-357.

Young, S., Sparks, R., Aspinall, W., Lynch, L., Miller, A., Robertson, R., Shepherd, J., 1998. Overview of the eruption of Soufrière Hills Volcano, Montserrat, 18 July 1995 to December 1997. Geophys. Res. Lett. 25, 3389-3392.

Zhang, Y., 1999. A criterion for the fragmentation of bubbly magma based on brittle failure theory, Nature 402, 648-650.

Figure captions

Figure 1: Topographic map of the South of Montserrat Island (Lesser Antilles) and sampling

locations in gray.

Figure 2: Macroscopic photographs of clasts covering the range of erupted materials during

the 1997 Vulcanian explosions. A) Dense and glassy clast. B) Homogeneous

pyroclastic flow pumice. C) and D) Heterogeneous pyroclastic flow pumice with

dense and vesicular textures. E) Breadcrusted bomb in cross section showing the

difference between core and crust. F) Homogeneous fallout pumices with angular and

curviplanar shapes.

Figure 3: SEM backscatter electron images (various scales) showing representative textural

characteristics of the 1997 Vulcanian pumices. A) Dense clast with a micro-

crystallized groundmass. B) Homogeneous pyroclastic flow pumice. C) and D)

Heterogeneous pyroclastic flow pumices. The dense parts of the pumices are

illustrated in the bottom-left part of the images and the vesicular parts are illustrated in

the top-right part. E) Homogeneous fallout pumice. F) Breadcrusted bomb. The crust

is illustrated by the bottom-left part of the image and the core is illustrated by the top-

right part. Abbreviations: (Bu) bubble, (Gl) interstitial glass, (Pl) plagioclase, (Opx)

orthopyroxene, (Amph) amphibole, and (Si) silica precipitate. A), C), D), and F): scale

bar = 50 μm; B) and E): scale bar = 20 μm.

Figure 4: Schematics of a two step decompression model showing the pre-explosive magma

(left) and the clast at quench time after the explosion (right). Prior to explosion, the

magma is at pressure, P_i, porosity, α_i, and water distributed as exsolved, x_i, and

dissolved, s_i. The clast is quenched at pressure P_q, porosity α_q, and dissolved water

content, s_q. Its exsolved water content can be viewed as having either *1)* a pre-

explosive component, x_i, and a syn-explosive component, $x_{d1} + x_{d2}$, or *2)* an outgassed

component, x_{out}, and a leftover component made of pre-explosive vesicles, x_{q1}, connected, syn-explosive vesicles, x_{q2}, and isolated, syn-explosive vesicles, x_{d1}. Crystal weight fraction is unaffected by explosion and does not enter the mass balance.

Figure 5: Interstitial glass water content vs. sample bulk vesicularity. Errors in interstitial glass water content (shaded areas) are propagated from the uncertainties in glass proportion estimation and Karl-Fischer Titration. Errors in vesicularity measurements are ±5%. Symbols represent the five textural types studied herein and the shaded areas represent errors attached to each type. Cores and crusts of breadcrusted bombs are linked with a stippled line and their errors are shown with bars for graph readability.

Figure 6: Comparison between pressures calculated from interstitial glass H_2O content (Table 1) and from feldspars microlites volume proportion using the procedure described by Clarke et al. (2007).

Figure 7: Pre-explosive pressures and porosities, assuming clasts quenched instantly. Data are from Clarke et al. (2007) and this study. A) Vesicularity as a function of pre-explosive pressure. The thick line shows porosities achievable in the column starting with 4.6 wt% melt water content in the reservoir and degassing in closed system. The thin (dashed) line shows closed system degassing with an additional 2 wt% or 6 wt% exsolved water in the reservoir. B) Pre-explosive gas content as a function of pre-explosive pressure. The gray shaded box spans the amount of gas necessary to drive the Vulcanian jets (data from Formenti et al., 2003, the darkest part of the gradient represents higher frequencies).

Figure 8: Influence of the model free parameters on the ratio between water outgassed and water left in the connected vesicles at quench time (x-axis) and on the ratio between

pre-explosive and quench porosity (y-axis). Data points each represent one sample, and are divided in four symbols that each represents a quench pressure scenario (one is atmospheric with $H=0$ and three are fragmentation thresholds with H values of 0.2, 1, and 2). Dotted lines indicate ratios of one and divide the graph in four areas according to whether sample inflate/deflate and outgas massively/weakly, respectively. The gray areas behind each quench pressure scenario cover output ranges when varying the degassing constants E and F.

Figure 9: Pre-explosive pressures and porosities from a typical quench pressure scenario ($E=1.9$, $F=0.5$, $G=2.7$, and $H=1$). Data are from Clarke et al. (2007) and this study. When data are from this study, symbols represent lithology. The thick line shows porosities achievable in the column starting with 4.6 wt% melt in the reservoir and closed-system degassing. Errors bars represent analytical uncertainty and are based on maximum and minimum outputs values using the uncertainties on glass water content ($wt_{H2O\,q}$, our study), pre-explosive pressure (P_i, Clarke et al., 2007) and vesicularity (α_q, both studies) in Table 1. The gray area represents model uncertainty and is based on outputs using the constrained ranges of the free parameters.

Figure 10: Pre-explosive gas content as a function of pre-explosive pressure. The gray shaded box spans the amount of gas necessary to drive the Vulcanian jets (data from Formenti et al., 2003, the darkest part of the gradient represents higher frequencies). Data are from Clarke et al. (2007) and this study. Errors bars represent analytical uncertainty and are based on maximum and minimum outputs values using the uncertainties on glass water content ($wt_{H2O\,q}$, our study), initial pressure (P_i, Clarke et al., 2007) and vesicularity (α_q, both studies) in Table 1.

Figure 11: Pressure from glass water content vs. pressure from a typical model output ($E=1.9$, $F=0.5$, $G=2.7$, and $H=1$). The 1:1 line falls outside data errors, which implies

that our two-step decompression model introduces significant corrections on pre-explosive pressure estimates. Data are from Clarke et al. (2007) and this study.

Figure 12: Pressure evolution from pre-explosive to quench. For each sample, the circle represents P_i, the arrow indicates decompression, and the free end marks P_q. Gray areas indicate the span of maximum instant overpressure each sample can bear pre-explosively.

Figure A1: Water solubility experiments obtained at <75 MPa and 1040°C starting from the rhyolitic interstitial glass of the 1997 Vulcanian pumices and comparison with predicted solubilities from Liu et al. (2005) model with pure H_2O (continuous line).

Table 1. Summary of textural features, bulk and corrected H_2O contents in interstitial glasses, and pre-explosive pressures. All clasts are from pyroclastic flow deposits except when mentioned. Vesicularities are bulk, glass proportions are given on a bubble-free basis. Phenocryst contents are thus equal to 100% minus interstitial glass contents. Bulk microlite contents were measured irrespective of mineralogy whereas plagioclase microlite contents consist of plagioclase crystals <500 μm^2. Microlite contents (bulk and plagioclase) are given with respect to the groundmass.

Samples	Vesicularity[a] (vol. %)	Interstitial glass[a] (vol. %)	Bulk microlite (vol. %)	Plag. microlite (vol. %)	Bulk H_2O[b] (wt. %)	Glass H_2O[c] (wt. %)	Pressure[d] (MPa)
Dense clasts							
AMO27	< 5	51 (3)	39	29	0.18 (0.06)	0.37 (0.13)	1.3 (0.88)
AMO35[e]	< 5	53 (18)	51	51	0.10 (0.003)	0.20 (0.07)	0.39 (0.27)
AMO40	10	40 (7)	46	42	0.09 (0.02)	0.26 (0.06)	0.65 (0.29)
Homogeneous pumices							
AMO26	69	49 (10)	20	16	0.53 (0.08)	1.18 (0.30)	11.8 (5.5)
AMO29	52	47 (10)	32	25	0.20 (0.12)	0.45 (0.31)	1.9 (2.5)
AMO30	40	41 (15)	23	14	0.28 (0.04)	0.74 (0.33)	4.9 (4.1)
AMO32	40	41 (10)	21	16	0.29 (0.04)	0.77 (0.21)	5.2 (2.7)
AMO33	51	40 (4)	22	18	0.81 (0.10)	2.19 (0.35)	36.3 (10)
AMO42	35	53 (4)	35	32	0.19 (0.01)	0.45 (0.04)	1.9 (0.32)
AMO43	25	41 (10)	22	19	0.19 (0.06)	0.54 (0.19)	2.7 (1.8)
PV3	61	63 (5)	16	13	0.80 (0.05)	1.32 (0.14)	14.5 (2.8)
Breadcrusted bombs (co = core and cr = crust)							
BCP1-co	44	40 (12)	27	18	0.41 (0.01)	1.10 (0.34)	10.3 (5.9)
BCP1-cr	6	46 (3)	31	27	0.36 (0.05)	0.83 (0.13)	6.1 (1.8)
BCP2-co	31	58 (10)	32	19	0.50 (0.05)	1.16 (0.15)	11.4 (2.7)
BCP2-cr	< 5	53 (10)	36	26	0.44 (0.07)	0.99 (0.19)	8.5 (3.0)
BCP3-co[f]	8	30 (4)	nd	nd	0.35 (0.09)	1.15 (0.30)	11.2 (5.4)
BCP3-cr[f]	< 5	40 (11)	nd	nd	0.28 (0.13)	0.63 (0.42)	3.6 (4.6)
BCP4-co	54	39 (10)	35	19	0.59 (0.01)	1.63 (0.41)	21.3 (9.7)
BCP4-cr	< 5	49 (10)	37	27	0.37 (0.04)	0.81 (0.18)	5.8 (2.4)
Homogeneous pumices from fallout							
AMO3C	55	37 (4)	19	16	0.45 (0.03)	1.35 (0.12)	15.2 (2.5)
AMO3D	65	38 (4)	12	8	0.77 (0.04)	2.19 (0.19)	36.3 (5.6)
AMO6A-1	62	36 (4)	19	14	0.63 (0.19)	1.93 (0.61)	28.9 (16)
AMO6A-2	60	38 (4)	14	11	0.56 (0.05)	1.65 (0.17)	21.8 (4.1)
AMO9	68	35 (4)	11	7	0.90 (0.04)	2.79 (0.33)	55.7 (12)
MT6-03	57	36 (1)	12	9	0.79 (0.03)	2.38 (0.12)	42.1 (3.8)
MT6-04	67	30 (2)	17	12	0.49 (0.01)	1.77 (0.12)	24.7 (3.0)
Heterogeneous pumices (D = dense part of the clast and V = vesicular part of the clast)							
AB1-D	9	39 (4)	33	25	0.20 (0.03)	0.49 (0.09)	2.2 (0.79)
AB1-V	45	42 (4)	35	29	0.28 (0.04)	0.78 (0.14)	5.4 (1.8)
AB2-D	8	26 (5)	30	24	0.14 (0.06)	0.73 (0.29)	4.8 (3.6)
AB2-V	38	42 (5)	30	23	0.38 (0.06)	0.97 (0.19)	8.2 (3.0)
AMO34-D	29	40 (11)	43	31	0.11 (0.004)	0.29 (0.08)	0.80 (0.43)
AMO34-V	38	38 (4)	39	32	0.31 (0.01)	0.88 (0.09)	6.8 (1.3)
AMO38-D	22	32 (1)	34	28	0.15 (0.02)	0.48 (0.06)	2.1 (0.51)
AMO38-V	44	35 (1)	27	21	0.45 (0.07)	1.38 (0.22)	15.7 (4.6)
AMO44-D	< 5	52 (7)	41	30	0.14 (0.01)	0.33 (0.04)	1.0 (0.24)
AMO44-V	38	43 (4)	38	32	0.23 (0.03)	0.67 (0.08)	4.1 (0.92)
SP1-D	24	36 (2)	34	24	0.30 (0.06)	0.91 (0.17)	7.2 (2.5)
SP1-V	51	43 (4)	23	16	0.44 (0.004)	1.10 (0.10)	10.3 (1.8)

n.d.: not determined.

[a] Measured by SEM image analysis, 1σ in parenthesis.

[b] Median of up to 3 Karl-Fischer titrations on >50 mg samples, 1σ in parenthesis.

[c] Corrected using the bulk H_2O content and the crystallinity of each sample, error in parenthesis.

[d] Calculated using Liu et al. (2005) solubility model at 850°C and $P_{CO2} = 0$, error in parenthesis.

[e] Interstitial glass content roughly estimated because of pervasive small (<1μm) microlites.

[f] Sample with angular bubbles and crushed phenocrysts, which caused difficulties in image analysis.

Table 2. Summary of pre-explosive (*i* indices) and quench (*q* indices) pressures and quantities of water and gas for the best-fit scenario with adjusted quench pressure and outgassing. Symbols as in the text. Other variables are calculated as follow: $x_{d1}=F\,x_{q1}$, $x_{out}=G\,x_{q1}$, $x_{q2}=(E-F)x_{q1}$, and $x_{q2}=(E-F)x_i$ with $E=1.9$, $F=0.5$, and $G=2.7$. Negative s_q values are discussed in the text.

Samples	P_i MPa	s_i wt%	x_i ppm	α_i vol%	P_q MPa	s_q wt%	x_{q1} ppm
Clarke et al. (2007)							
990302-5a	7.2	0.90	3303	37	3.4	0.36	1554
990302-6a	7.2	0.90	2492	31	3.7	0.50	1173
990302-6b	24.7	1.76	5604	22	3.1	0.84	2637
990302-7a	2.8	0.56	548	20	2.8	0.47	258
990302-7b	7.2	0.90	3419	38	3.3	0.34	1609
990329-1a	3.0	0.57	1608	40	3.0	0.31	757
990329-1b	13.7	1.27	3812	26	3.3	0.65	1794
990329-2a	3.2	0.59	6930	73	3.0	-0.54	3261
990329-3a	8.7	1.00	6206	48	3.0	-0.02	2920
990329-3b	6.0	0.82	5340	53	3.1	-0.05	2513
990329-3c	3.9	0.65	3961	57	3.2	0.004	1864
990329-4a	9.6	1.06	4119	35	3.2	0.38	1938
990329-4b	4.1	0.67	5340	62	3.1	-0.20	2513
99302-2	2.3	0.50	656	27	2.3	0.39	309
99303-2	2.2	0.49	224	11	2.2	0.45	105
99305-3	5.1	0.76	3419	46	3.3	0.20	1609
99305-3 3p	3.4	0.61	654	20	3.4	0.50	308
99305-3 4p	1.3	0.37	755	42	1.3	0.25	355
99306-1a1	5.6	0.79	566	11	5.6	0.70	266
99306-1a2	0.9	0.30	49	7	0.9	0.29	23
99318-1a	1.8	0.44	79	5	1.8	0.43	37
99323-1c	5.6	0.79	1467	25	5.4	0.55	690
99623-1c	2.1	0.47	37	2	2.1	0.47	18
Dense clasts							
AMO27	1.3	0.38	41	4	1.3	0.37	19
AMO35	0.4	0.20	12	4	0.4	0.20	6
AMO40	0.7	0.27	44	8	0.7	0.26	21
Homogeneous pumices							
AMO26	26.7	1.84	4119	16	3.2	1.17	1938
AMO29	6.1	0.83	2356	33	3.8	0.45	1109
AMO30	9.0	1.02	1742	20	4.5	0.74	820
AMO32	9.5	1.05	1742	19	4.5	0.77	820
AMO33	47.8	2.55	2292	6	3.8	2.18	1078
AMO42	3.7	0.63	1135	28	3.7	0.45	534
AMO43	4.0	0.66	767	20	4.0	0.54	361
PV3	26.0	1.81	3088	13	3.4	1.31	1453
Breadcrusted bombs (crusts)							
BCP1-cr	6.6	0.87	244	4	6.6	0.83	115
BCP2-cr	9.2	1.03	280	4	9.2	0.99	132
BCP3-cr	3.8	0.65	116	4	3.8	0.63	54
BCP4-cr	6.2	0.84	189	4	6.2	0.81	89
Homogeneous pumices from fallout							
AMO3C	24.7	1.76	2565	12	3.6	1.34	1207
AMO3D	54.6	2.75	3542	8	3.3	2.17	1667
AMO6A-1	44.1	2.44	3192	8	3.4	1.91	1502

AMO6A-2	34.6	2.13	2990	10	3.5	1.64	1407
AMO9	79.6	3.41	3961	6	3.2	2.76	1864
MT06-03	56.6	2.81	2722	6	3.6	2.36	1281
MT06-04	42.2	2.38	3812	10	3.3	1.75	1794
Heterogeneous pumices							
AB1-D	2.4	0.51	138	7	2.4	0.49	65
AB1-V	10.3	1.10	1962	20	4.2	0.78	923
AB2-D	5.3	0.77	267	6	5.3	0.73	126
AB2-V	12.9	1.24	1666	14	4.7	0.97	784
AMO34-D	1.0	0.33	243	23	1.0	0.29	114
AMO34-V	11.2	1.15	1666	16	4.7	0.88	784
AMO38-D	2.8	0.55	452	17	2.8	0.48	213
AMO38-V	22.7	1.69	1914	10	4.2	1.37	901
AMO44-D	1.1	0.34	32	4	1.1	0.33	15
AMO44-V	7.7	0.94	1666	22	4.7	0.67	784
SP1-D	10.6	1.11	1259	13	6.9	0.91	592
SP1-V	17.7	1.47	2292	14	3.8	1.09	1078

Table A1: Average composition of natural interstitial glass and composition of the rhyolitic

melt (wt%) used for H_2O solubility experiments

Sample[a]	SiO_2[c]	Al_2O_3	TiO_2	FeO	MgO	MnO	CaO	Na_2O	K_2O	Total
Natural composition (19)[b]	78.66 (2.18)	11.20 (1.07)	0.39 (0.11)	1.93 (0.25)	0.30 (0.10)	0.10 (0.07)	1.48 (0.58)	3.57 (0.22)	2.38 (0.34)	100
VH (16)[b]	78.67 (0.34)	11.44 (0.13)	0.36 (0.05)	2.11 (0.15)	0.29 (0.04)	0.12 (0.07)	1.71 (0.10)	3.27 (0.13)	2.04 (0.07)	100

[a] All glasses were analyzed using a Cameca SX50 microprobe with a ~10-µm-diameter defocused beam and 6 nA beam current at 15kV (counting time : 10s). Glass compositions are normalized to anhydrous compositions.
[b] Number of microprobe analyses.
[c] Number in brackets are 2σ.
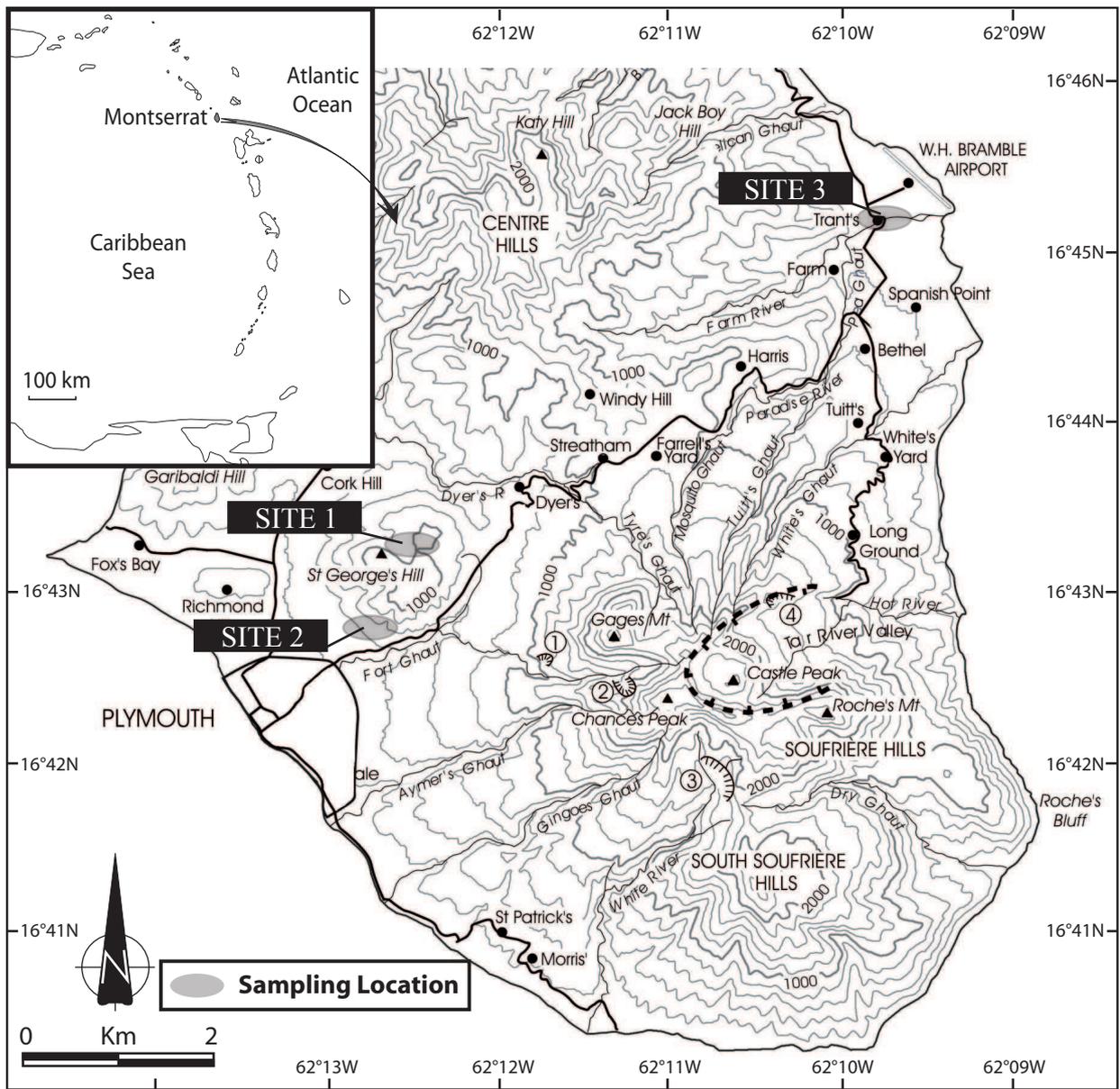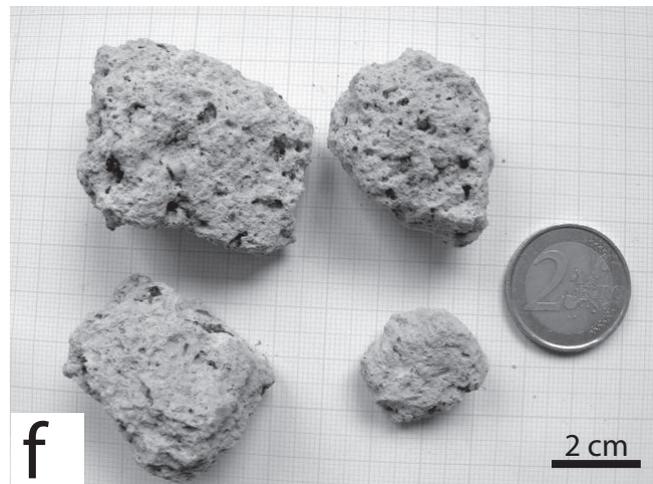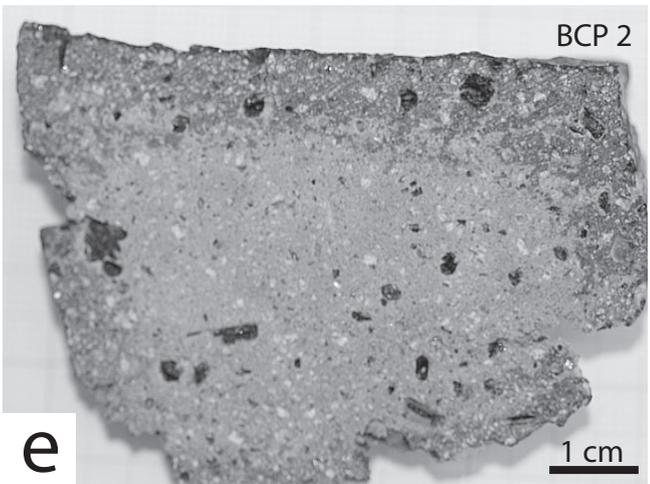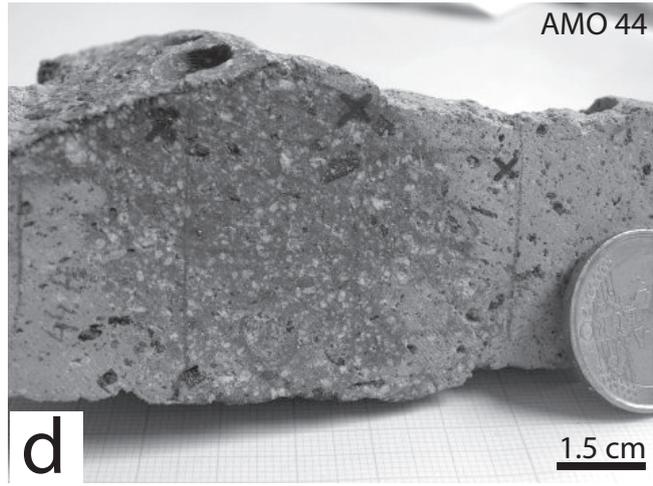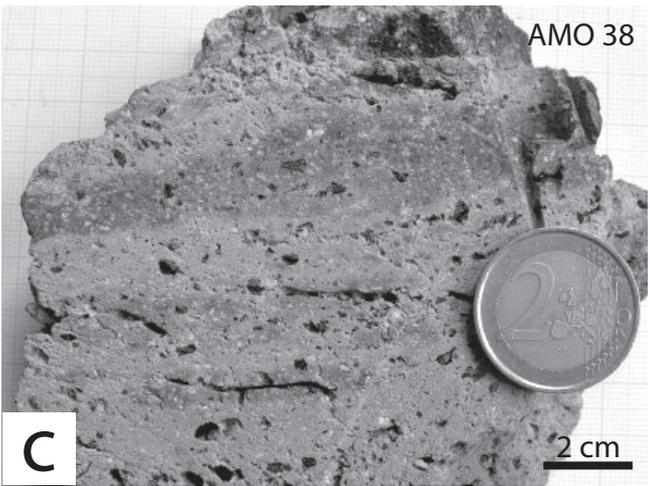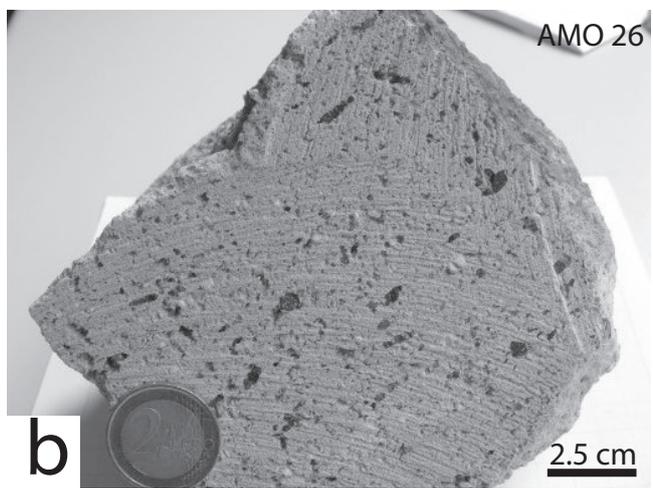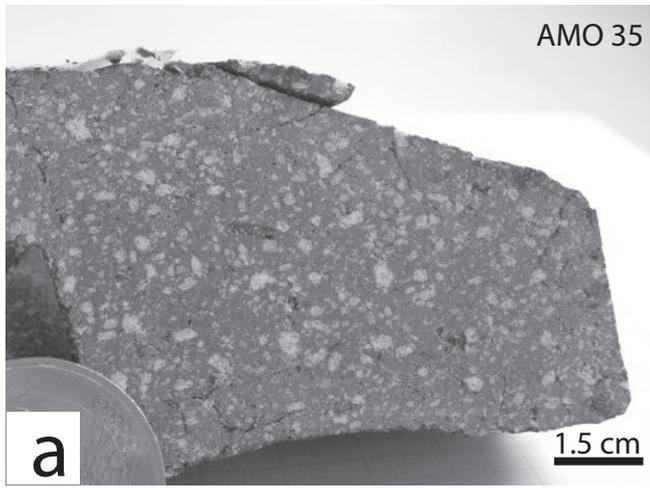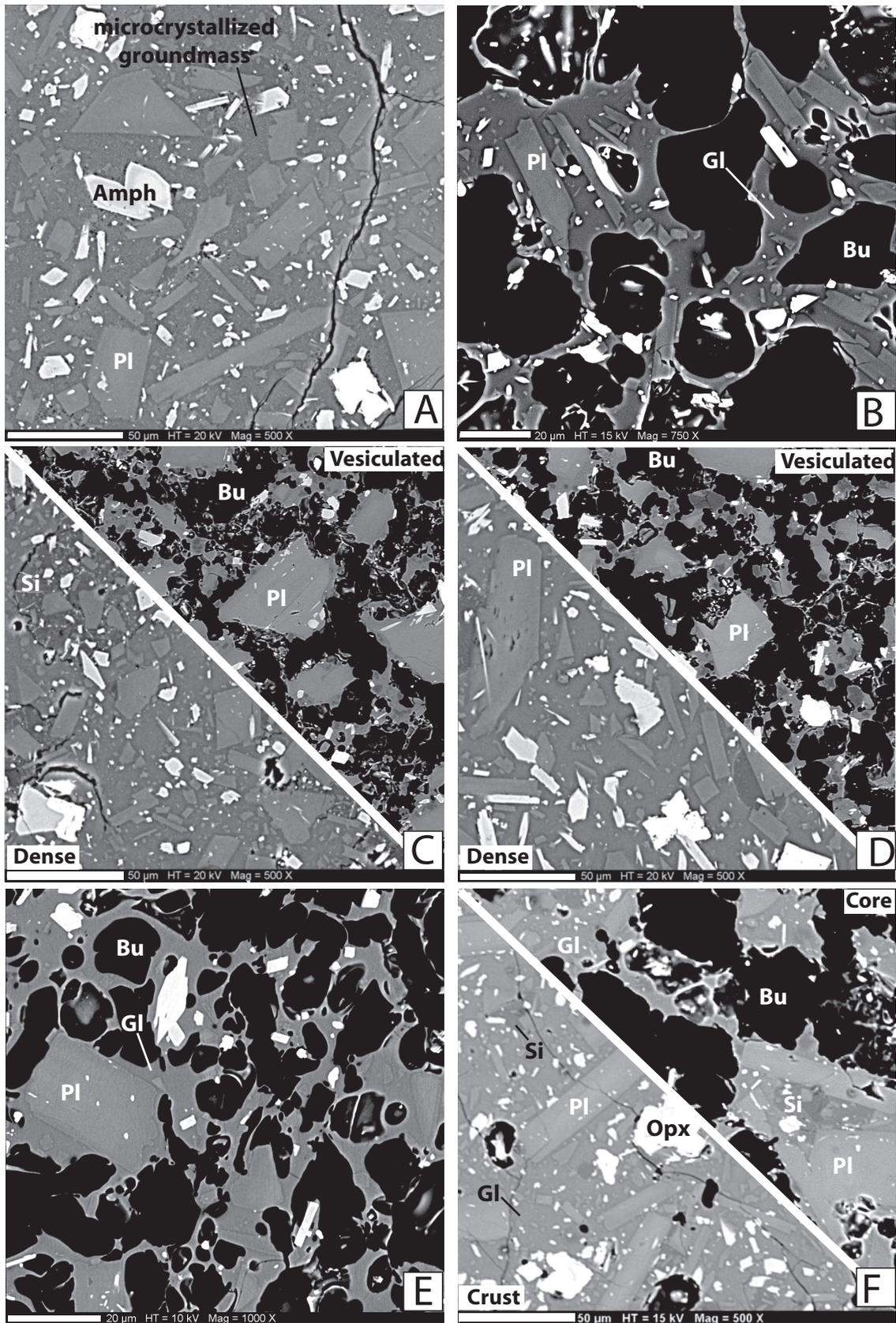
FIGURE 1

FIGURE 2

FIGURE 3
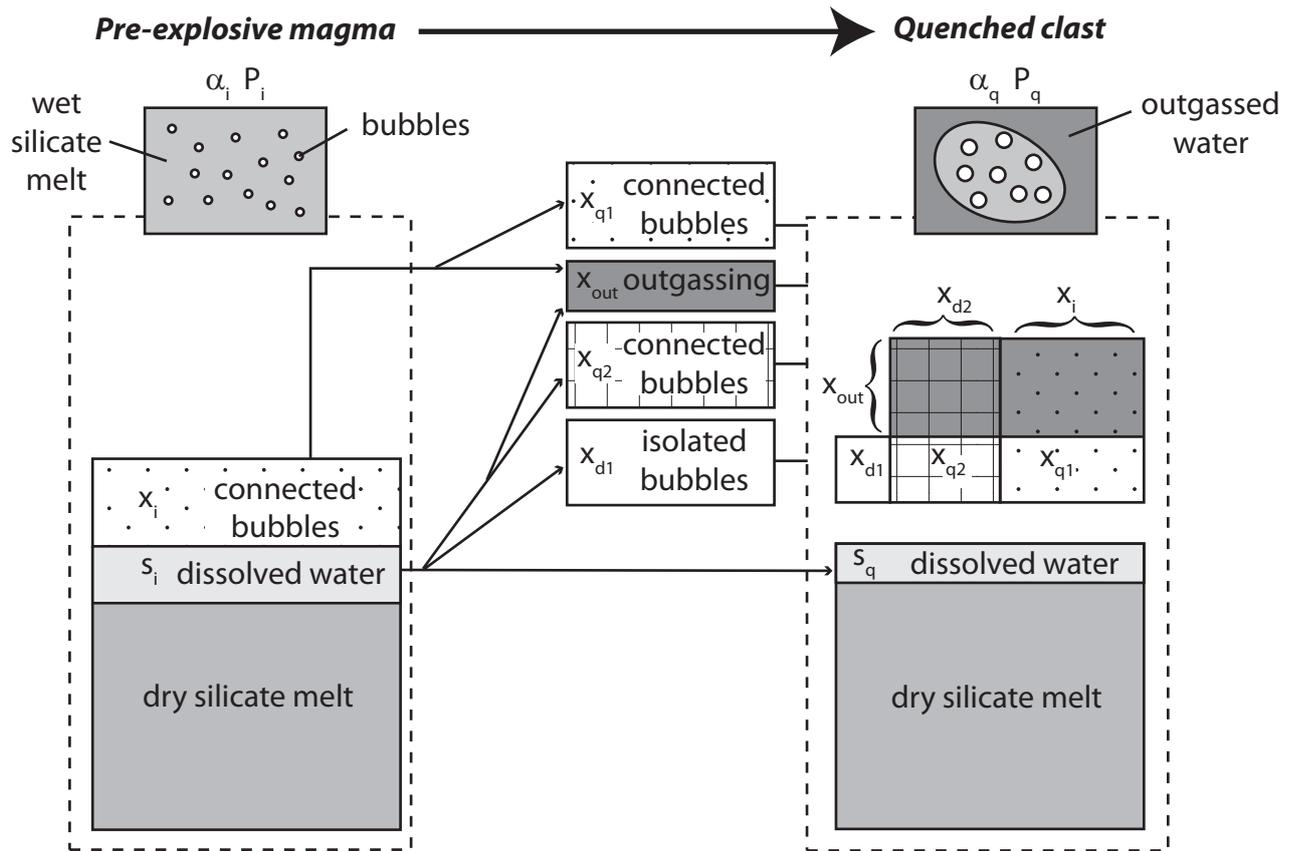
**FIGURE 4**
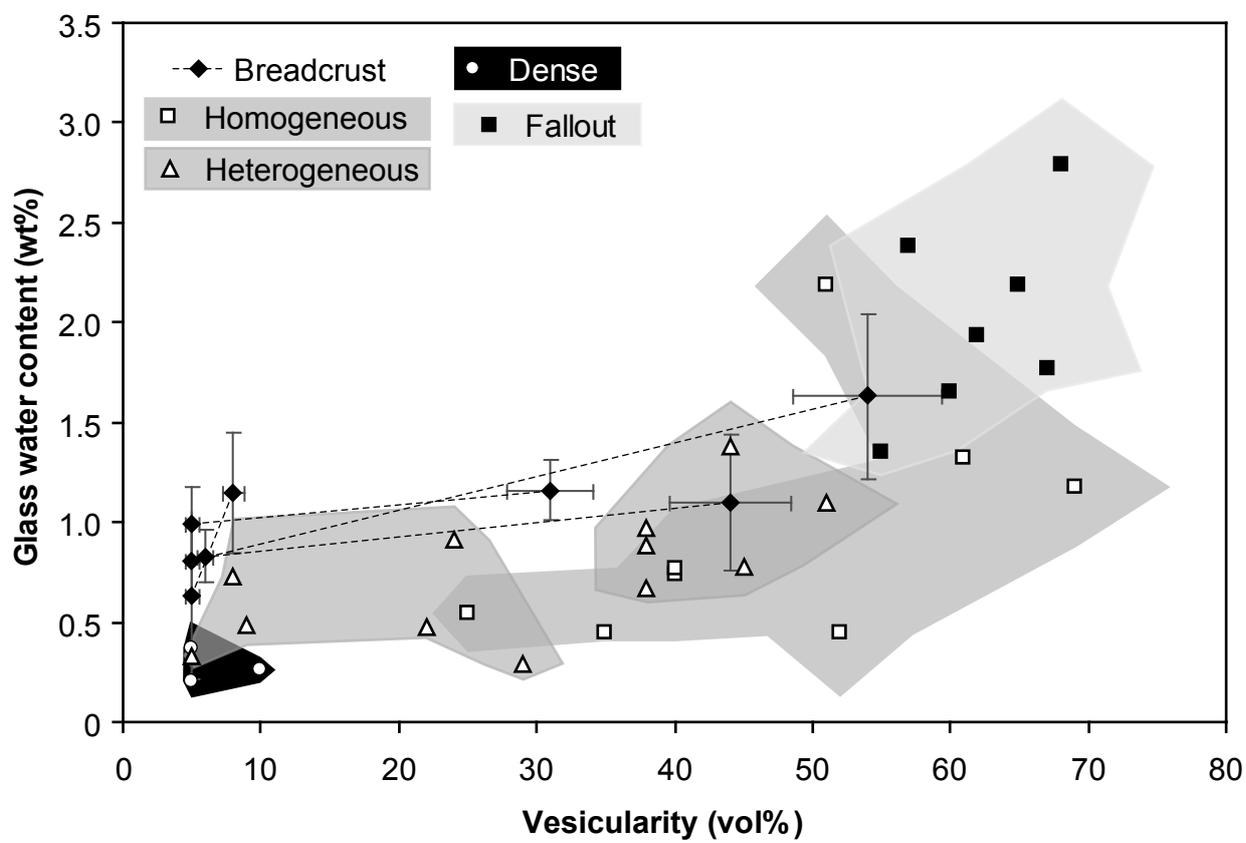
FIGURE 5
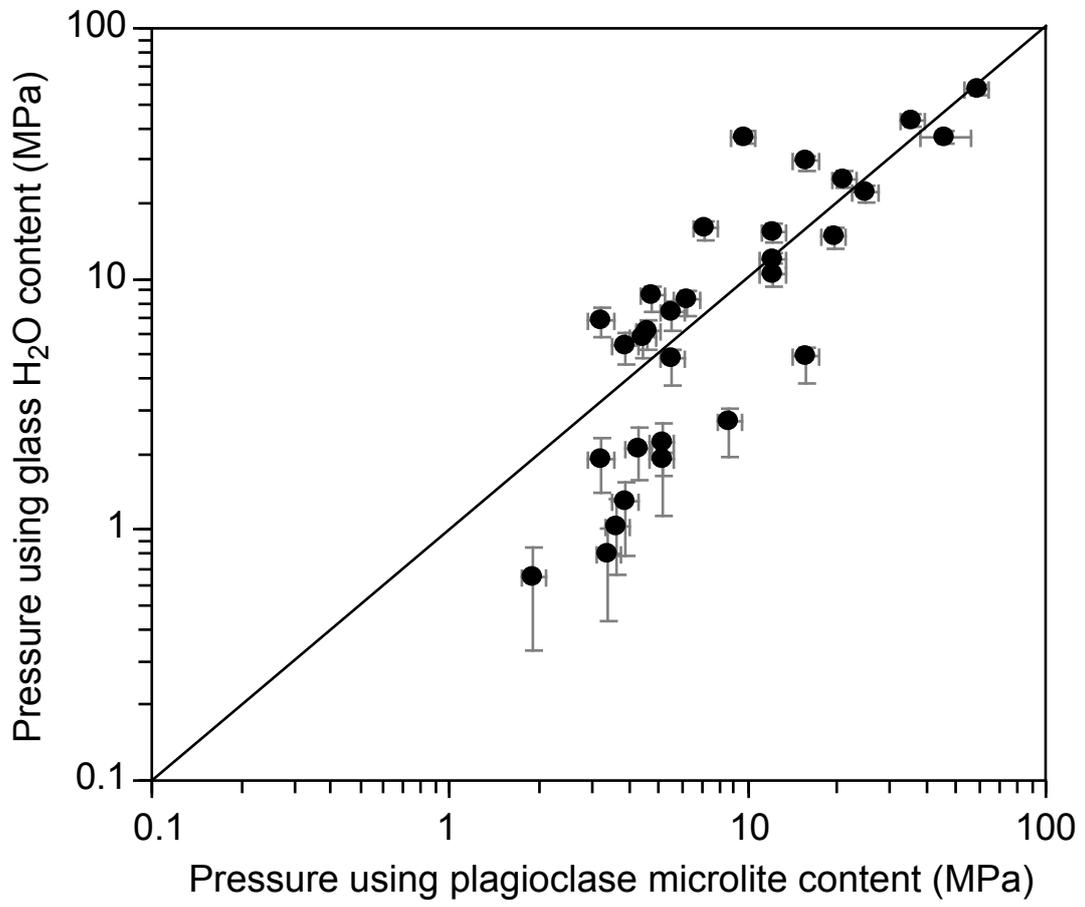
FIGURE 6
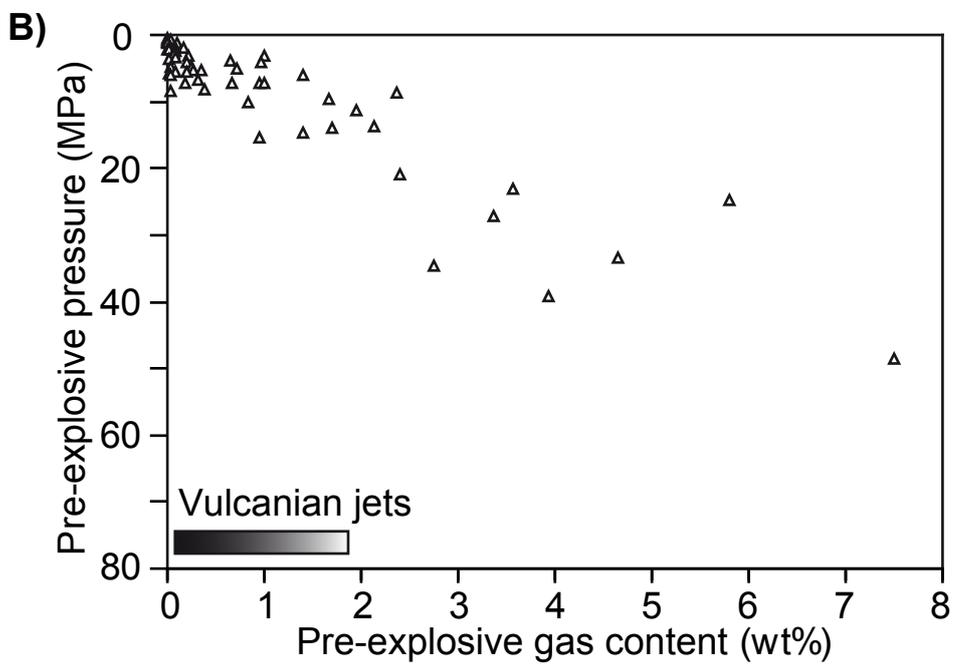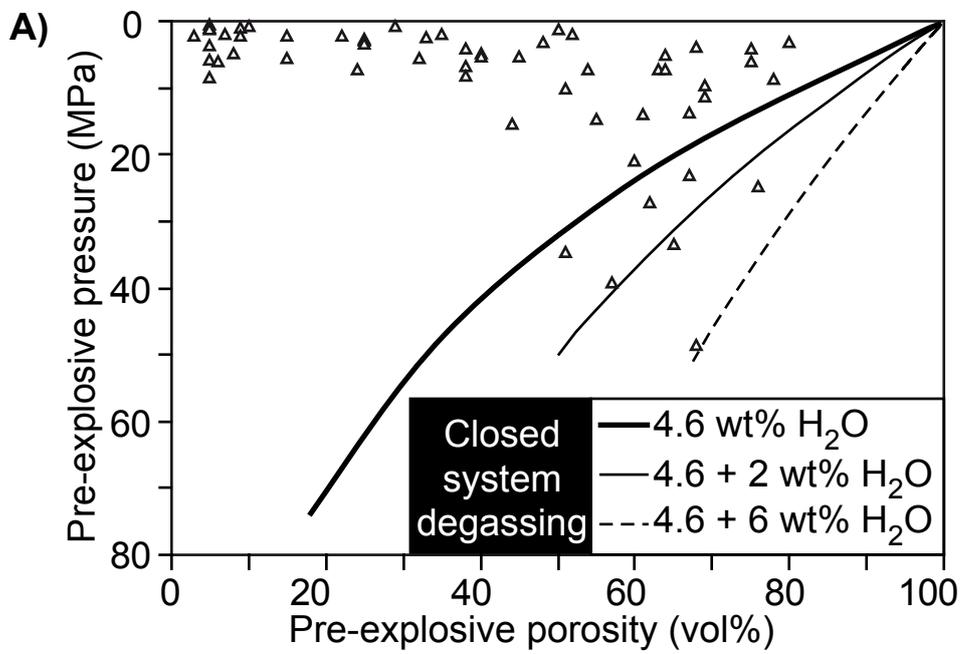
FIGURE 7
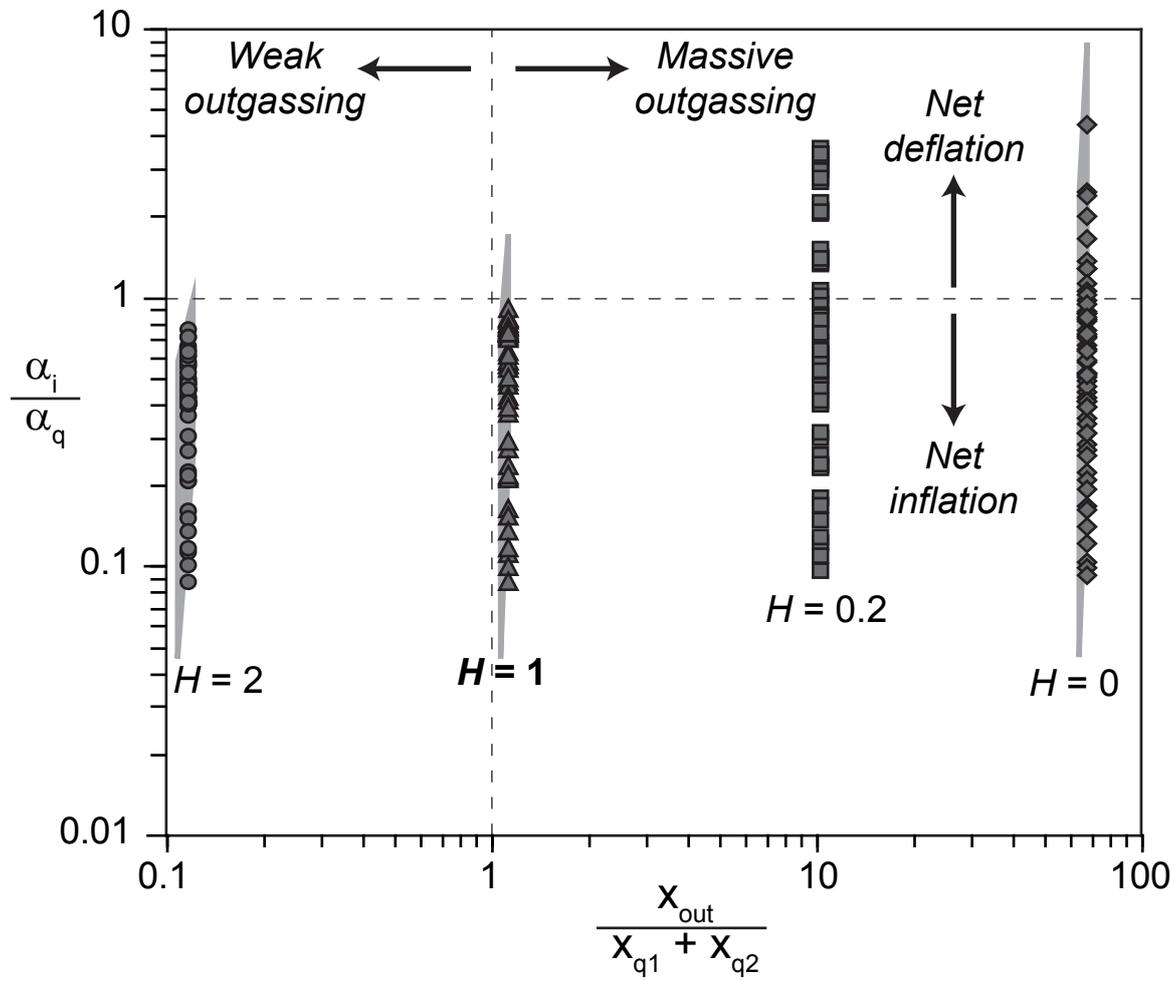
FIGURE 8
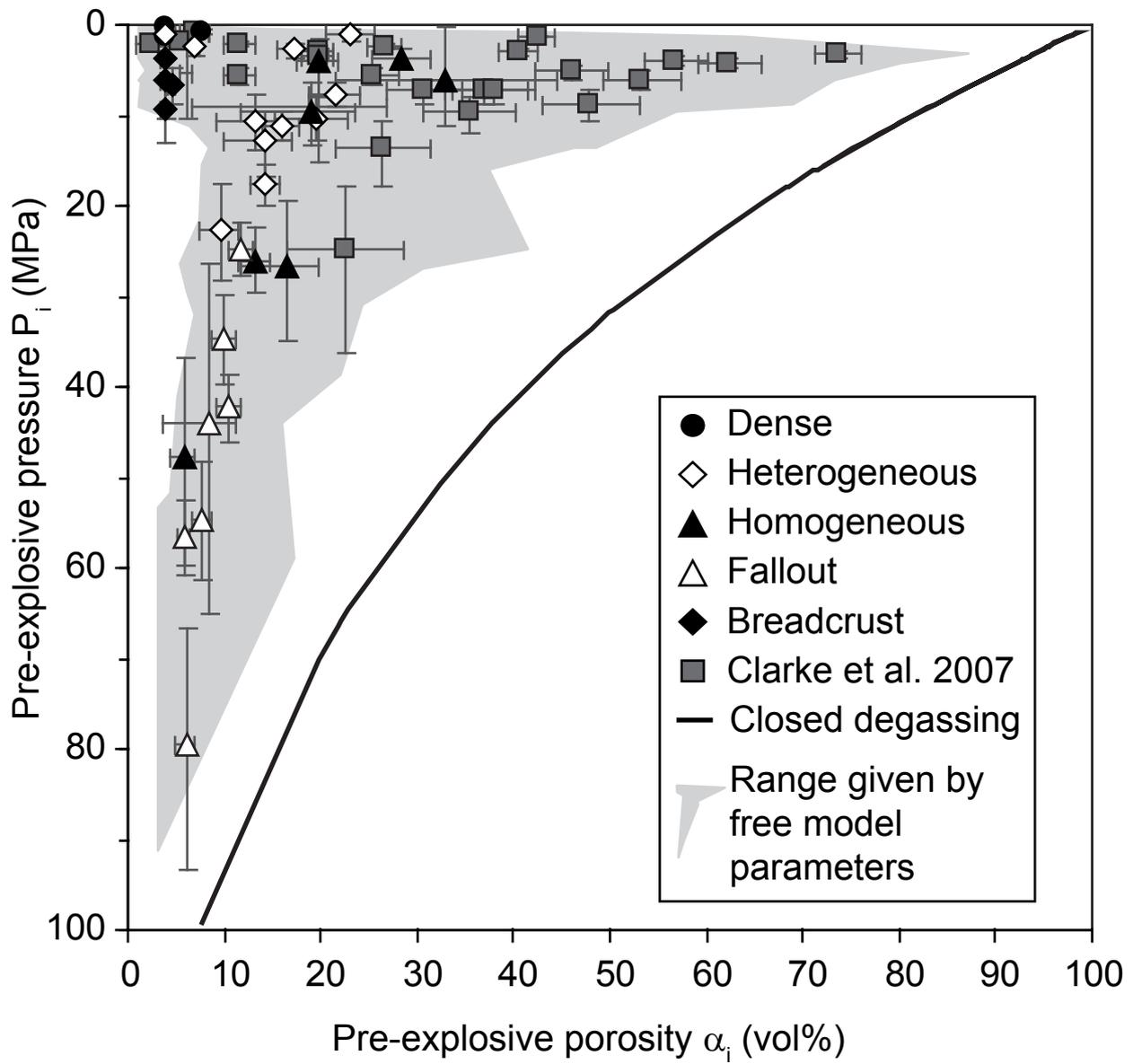
FIGURE 9
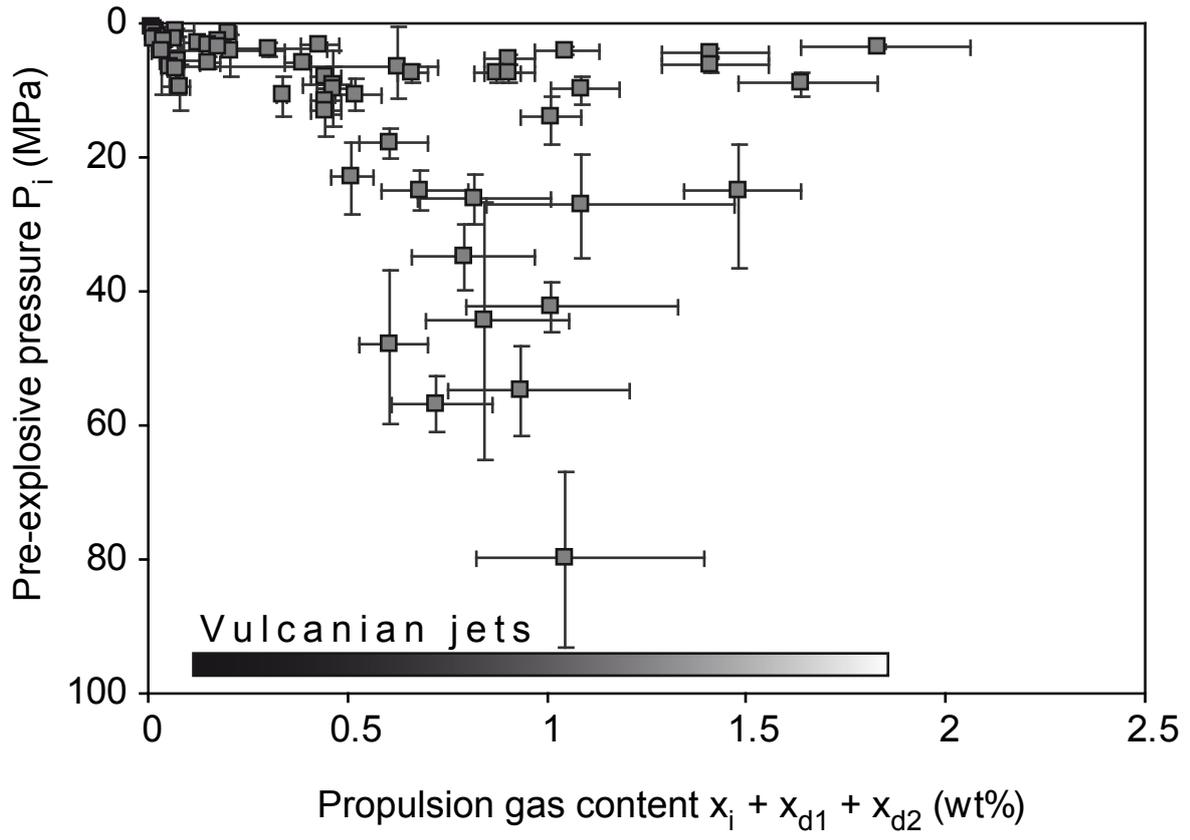
FIGURE 10
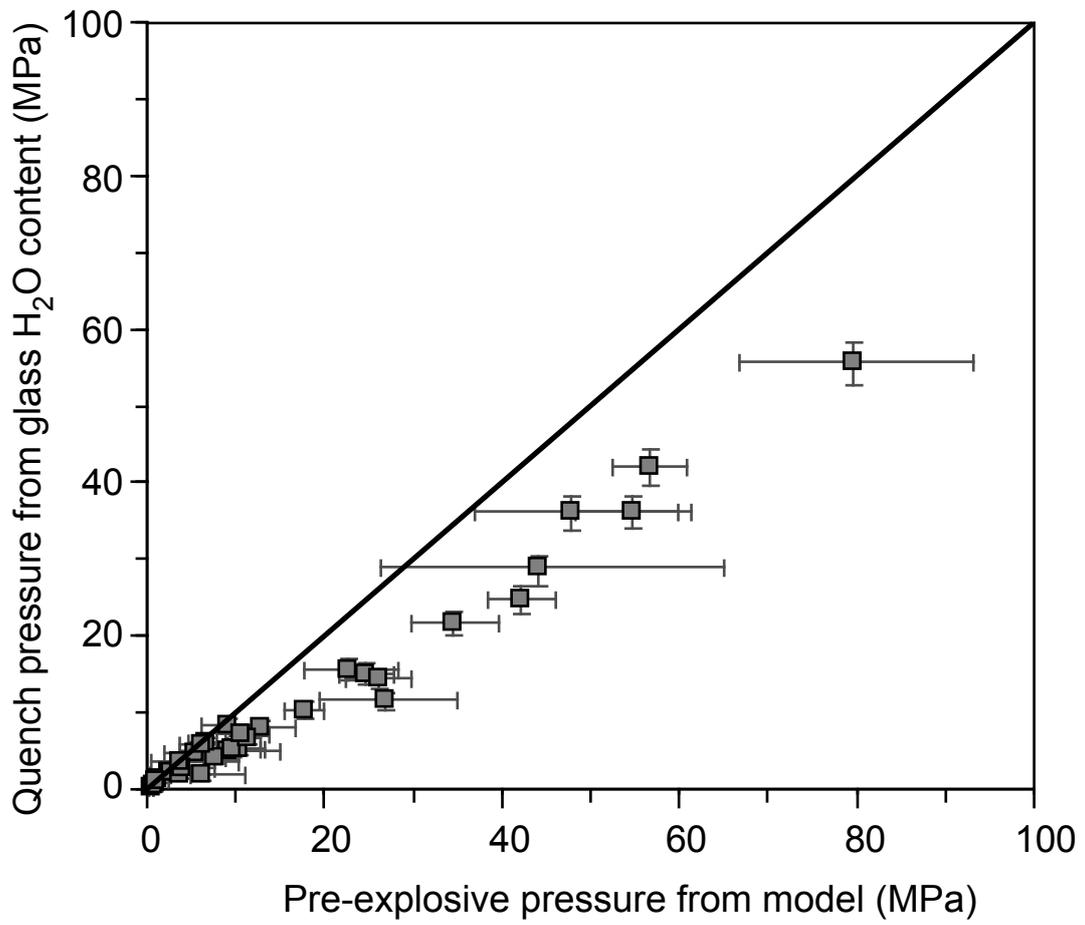
FIGURE 11

FIGURE 12

FIGURE A1